Energy dependence of the fusion and elastic scattering of $^{16}O+^{40}Ca$

S. E. Vigdor
Physics Division, Argonne National Laboratory, Argonne, Illinois 60439
and Department of Physics, Indiana University, Bloomington, Indiana 47405

D. G. Kovar and P. Sperr*
Physics Division, Argonne National Laboratory, Argonne, Illinois 60439

J. Mahoney, A. Menchaca-Rocha,† C. Olmer,‡ and M. S. Zisman
Lawrence Berkeley Laboratory, Berkeley, California 94720

(Received 16 July 1979)

In a study of the system $^{16}O + ^{40}Ca$, the total evaporation-residue cross section has been measured at nine energies, and elastic-scattering angular distributions at five energies, within the range 40 MeV $\leq E_{lab} \leq$ 214 MeV. The fusion cross section is observed to saturate above $E_{lab} = 63$ MeV. Several possible mechanisms to explain this effect are considered, and the shortcomings of each are pointed out. The model based on a critical distance in the entrance channel is judged the most nearly acceptable. At the highest bombarding energies the fusion residues exhibit (1) angular distributions which suggest significant emission of energetic α particles (or larger clusters), and (2) total cross sections in conflict with expectations based on the vanishing of the rotating-liquid-drop model fission barrier. An optical model analysis of the elastic-scattering data is used to extract total reaction cross sections (σ_{reac}). The nonlinear dependence of σ_{reac} on $1/E_{c.m.}$ is noted and the implications for the extraction of "interaction barrier" and "fusion barrier" parameters are discussed. A method for unified analysis of low-energy elastic-scattering and fusion data, based on the assumption that a single potential is relevant to both, is suggested. Simultaneous fits to 56-MeV elastic-scattering and low-energy fusion measurements for $^{16}O + ^{40}Ca$ are attained with Woods-Saxon potentials only if the real well diffuseness is constrained to the range (0.50 ± 0.05) fm, a value not compatible with several proposed potentials based on liquid-drop model concepts. The real potentials preferred in this low-energy analysis are not capable of providing good optical model fits to the highest-energy elastic data.

[NUCLEAR REACTIONS Fusion and elastic scattering of $^{16}O+^{40}Ca$, $40 \leq E_{lab} \leq 214$ MeV; measured $\sigma_{fusion}(E)$, $\sigma_{elastic}(\theta, E)$; evaluation of various mechanisms for saturation of σ_{fusion} at high energies; optical model analysis of $\sigma_{elastic}$; simultaneous analyis of low-energy elastic and fusion data; deduced s-wave barrier parameters, real well diffuseness of nucleus-nucleus potential.]

I. INTRODUCTION

One of the features of heavy-ion collisions which is common to the entire range of projectiles which have been studied is the occurrence of very large cross sections for reactions other than complete fusion. Indeed, *no* clear evidence of appreciable compound-nucleus formation has been observed in those cases where the product Z_1Z_2 of the projectile and target atomic charges exceeds ~2500 (Refs. 1 and 2). In lighter systems, fusion cross sections (σ_{fus}) at bombarding energies five or more times the Coulomb barrier height (V_{B_0}) have been found to exhaust only roughly half of the total reaction cross section (σ_{reac}).[1,3-8] In place of fusion, one has observed partially or completely damped ("deeply inelastic") processes, characterized by extensive dissipation of relative kinetic energy, in conjunction with the modest mass transfer and strongly peaked angular distributions indicative of a short reaction time scale (10^{-21}–10^{-22} sec) (see Refs. 9–11, and references therein). It appears that the problem of understanding the conditions responsible for deeply inelastic collisions is inextricably connected with that of determining the nature of the physical limitation(s) on the fusion of heavy ions.

The models which have been proposed to explain why σ_{fus} is in some cases much smaller than σ_{reac} fall into two basic classes. The first class relates the limit on σ_{fus} to properties of the conservative and frictional forces governing the relative motion in the entrance channel; these models require that the colliding nuclei, in order to fuse, must penetrate to a certain critical separation[3,12-15] and/or dissipate sufficient kinetic energy and angular momentum to get "trapped" in a potential well.[15-19] The second class of models attributes the restriction to properties of the compound nucleus, e.g., the absence of states above a certain (yrast) spin at the appropriate excitation,[4,6,7] or the reduction (and eventual vanishing) of the fission barrier at

high spin.[20,21]

In order to test and choose among these models, it is important to establish the energy dependence of the fusion vs total reaction cross sections over a wide energy range and for a wide variety of systems. Relatively light composite systems are particularly relevant, since the existing data[5-8] show that for these cases one may observe a clear transition from a low-energy region ($V_{B_0} \lesssim E_{\text{c.m.}} \lesssim 2V_{B_0}$) in which $\sigma_{\text{fus}} \simeq \sigma_{\text{reac}}$ to a higher-energy region in which σ_{fus} saturates while σ_{reac} continues to climb rapidly with increasing energy. A further advantage in studying collisions of light nuclei is the feasible application of microscopic models, such as the time-dependent Hartree-Fock[22,23] or the time-dependent two-center shell-model[14] approach; in the latter, for example, the transfer of energy between relative and intrinsic degrees of freedom explicitly reflects changes in the nucleon configurations (i.e., particle-hole excitations) within the composite system.

On the other hand, there are significant disadvantages, from the point of view of both experiment and theory, for systems with composite mass substantially less than $A \simeq 50$, which have been the subjects of the most complete investigations to date.[5-8] First, at the high energies within the fusion saturation region, particle decay of such light compound nuclei may leave evaporation residues as light as or lighter than the projectile nucleus, making the experimental distinction between fusion products and transfer or inelastic products uncertain.[6,7] Another problem with such light systems is the doubtful applicability of macroscopic treatments (most notably, the rotating-liquid-drop model of Ref. 21) of high-spin nuclear structure, which form the basis for the compound-nucleus fusion-limitation models. Furthermore, for the purpose of distinguishing between the two classes of fusion-limitation models, it is most desirable to populate a given compound nucleus via several entrance channels which differ considerably in mass asymmetry, a situation not readily attainable for compound nuclei with A much less than 50. High-energy fusion cross sections for significantly different entrance channels to the same compound nucleus have thus far been published[24] only for ^{170}Yb (and a nearby system, Ref. 25) at a single excitation energy. The results of Refs. 24 and 25 indicate the importance of entrance-channel dynamics, but more systematic measurements, especially for lighter systems, are needed.

The present paper reports measurements of σ_{fus} over a broad range of bombarding energies (40 MeV $\leq E_{\text{lab}} \leq$ 214 MeV) for ^{16}O + ^{40}Ca, a system which retains the advantages but eliminates most objections to the study of lighter nuclei. For example, the same compound nucleus (^{56}Ni) can also be reached from easily accessible and suitably different entrance channels, namely, ^{20}Ne + ^{36}Ar, ^{32}S + ^{24}Mg, and ^{28}Si + ^{28}Si. At the present time, with appropriate experimental results for these alternative channels not yet available,[26] the ^{16}O + ^{40}Ca data do not allow us to comment *in a model-independent way* on the relative importance of entrance-channel vs compound-nucleus limitations on fusion. However, the ^{56}Ni high-spin yrast line which would be defined by the ^{16}O + ^{40}Ca fusion data in an yrast-limit model can be meaningfully compared to rotating-liquid-drop model[21] (RLDM) expectations; this is done in Secs. IV A and IV B. The strength measured for evaporation residues at the highest energies studied may also bear on the validity of the RLDM predictions of the spin-dependent fission barrier $B_f(J)$ for ^{56}Ni, in particular, on the predicted critical angular momentum (J_{cr}) at which $B_f(J)$ vanishes. The potential parameters extracted from a fit to the fusion measurements in the critical-distance model[3] are compared with various theoretical predictions[27-30] for the ion-ion potential (see Secs. IV A and IV E). Several other proposed models for the limitation to high-energy fusion are considered qualitatively in Sec. IV C, and their inadequacies in explaining various aspects of the present and previous measurements are pointed out.

In making comparisons between the experimental results and macroscopic expectations, one should keep in mind the unique microscopic structure of the ^{16}O + ^{40}Ca system: Both entrance-channel nuclei and the compound nucleus (at least in its low-spin, spherical incarnation) are doubly magic. The shell structure of the nuclei involved certainly seems to play an important role in the fusion process for lighter systems[5,31]; its significance in the present case has not yet been fully investigated.[32]

In addition to fusion cross sections, we have obtained angular distributions of the elastic scattering of ^{16}O + ^{40}Ca at E_{lab} (^{16}O) = 56, 75, 104, 140, and 214 MeV. An optical model analysis of the data at all energies is reported in Sec. IV D. No attempt is made to resolve potential ambiguities on the basis of the elastic-scattering data alone; emphasis is rather placed on extracting information from the optical model analysis which is not very sensitive to these ambiguities, e.g., the total reaction cross section, the partial-wave decomposition of σ_{reac}, and the approximate depths of the real and imaginary wells in the surface region.

Additional information on the real well in the surface region, namely, on the position and height of the s-wave potential barrier, is available from

low-energy fusion measurements. We show how the simplest prescription for extracting barrier parameters[1-3,11,12,33] yields misleading results. Using the more general prescription discussed in Sec. IV E, we are able to find Woods-Saxon potentials which account *simultaneously* for the low-energy elastic-scattering and fusion measurements. This simultaneous analysis significantly constrains the *diffuseness* of the real nuclear potential. The preferred values for $^{16}O+^{40}Ca$ are not compatible with several proposed nucleus-nucleus potentials[28-30] based on liquid-drop model concepts. A simultaneous analysis of fusion and elastic data has also been reported in Ref. 34.

II. EXPERIMENTAL TECHNIQUES AND MEASUREMENTS

The broad range of c.m. energies (from 1.25 to nearly 7 times the Coulomb barrier height) covered in the present experiment was attained by using ^{16}O beams from the Argonne National Laboratory (ANL) FN tandem accelerator at the lower energies and from the Lawrence Berkeley Laboratory (LBL) 88-inch cyclotron at the higher energies. Table I summarizes the energies and laboratories at which fusion and elastic-scattering data were acquired, along with information concerning the detection systems and ^{40}Ca targets. All measurements were made using silicon surface-barrier detector telescopes, in the 178-cm diameter scattering chamber at ANL and the 92-cm chamber at LBL. Enriched (>99%) ^{40}Ca targets, with thickness in the range of ~100–800 $\mu g/cm^2$, were used. The targets were self-supporting foils for all measurements at $E_{lab} \geq 75$ MeV; the 20–30 $\mu g/cm^2$ carbon backings for the targets used at the lower energies did not interfere appreciably with the identification of $^{16}O+^{40}Ca$ fusion residues, but did contribute ~10% of the observed counts in the elastic peak at those forward angles where the scattering from ^{12}C and from ^{40}Ca could not be resolved.

A. Fusion measurements

The fusion cross sections were measured by detecting the heavy fragments remaining after compound-nucleus formation and any subsequent particle emission in a two- or three-element telescope with a front counter thin enough (2.3 or 3.6 μm) to transmit $\gtrsim$90% of the evaporation residues. A system of two thin tantalum slits provided angular collimation for the fusion telescope and defined a solid angle in the range of $2-13\times10^{-6}$ sr corresponding to target-detector distances between 20 and 50 cm.

Representative two-dimensional (E_{total} vs ΔE) spectra obtained with the fusion telescope at E_{lab} =50, 140, and 214 MeV are shown in Fig. 1. These spectra present a clear overview of the total distribution of reaction strength. The strength for quasielastic and deeply inelastic processes is concentrated, at all energies, in the carbon, nitrogen, and oxygen lines which appear at low values of ΔE. The cross section for transfer products with $Z>8$ appears to spread toward higher Z with increasing bombarding energy, but remains fairly weak even at 214 MeV. The fusion residues are contained in the intense region corresponding to low E_{total} and the highest values of ΔE. The Z resolution in this region is not sufficient to separate lines corresponding to different elements, but it is nonetheless clear that the fusion strength extends to progressively lower values of Z as the bombarding energy increases, with an especially marked change between 140 and 214 MeV. At 214 MeV the experimental distinction between strength

TABLE I. Summary of measurements and apparatus used in $^{16}O+^{40}Ca$ study.

Laboratory	Bombarding energy [a] (MeV)	Fusion ΔE counter thickness (μm of Si)	Elastic telescope configuration	^{40}Ca target thickness ($\mu g/cm^2$)	Target backing
	39.6	2.3	b	110	20 $\mu g/cm^2$ C
	44.6	2.3	b	110	20 $\mu g/cm^2$ C
	49.7	2.3	b	110	20 $\mu g/cm^2$ C
ANL	55.6	3.6	ΔE-E-TOF	140	30 $\mu g/cm^2$ C
	62.7	3.6	b	90	20 $\mu g/cm^2$ C
	74.4	3.6	ΔE-E-TOF	400	none
	103.6	3.6	ΔE_1-ΔE_2-E	340	none
LBL	139.6	3.6	ΔE_1-ΔE_2-E	340800	none
	214.1	3.6	ΔE_1-ΔE_2-E	340800	none

[a] Energy at the center of the target is specified here. Nominal beam energies are used throughout the text.
[b] No elastic-scattering data were acquired at this energy.

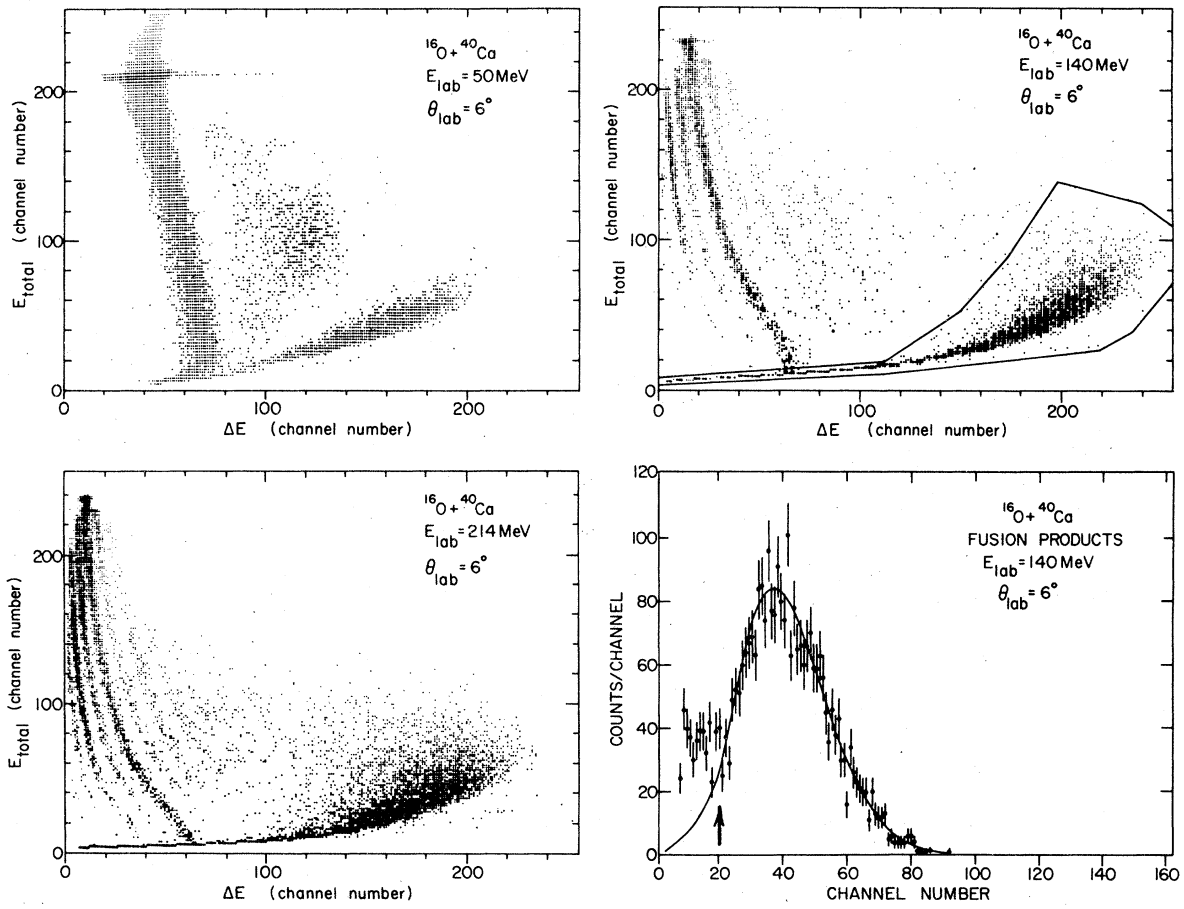

FIG. 1. Representative two-dimensional (E_{total} vs ΔE) spectra obtained with the fusion telescope at E_{lab} = (a) 50 MeV, (b) 140 MeV, and (c) 214 MeV. Since a carbon-backed ^{40}Ca target was used in the lower-energy measurements, an intense region corresponding to fusion products from $^{16}O+^{12}C$ is observed in (a), but not in (b) or (c). A typical software contour defining the region of $^{16}O+^{40}Ca$ fusion residues is shown in the 140-MeV spectrum (b). The projected total-energy spectrum for all events within the contour in (b) is shown in (d). Channels to the left of the arrow in (d) comprise exclusively particles stopped in the ΔE counter. The number of stopped fusion residues is estimated from the area under the extrapolated portion of the smooth curve drawn through the data in (d).

spreading downward from the compound nucleus and upward from the projectile has begun to blur. We have estimated that this blur introduces about a ±4% systematic uncertainty in the counts attributed to fusion at 214 MeV; we have attempted to choose the lower limit ($Z \gtrsim 22$) consistently so as to include in the fusion region only those Z groups for which events were detected with E pulses extending all the way down to zero. In the spectra of Fig. 1, particles stopped in the front counter fall along the gently sloping straight line ($E_{total} = \Delta E$) near the bottom of the plot, with intercept at the origin.

Operationally, the fusion region was defined by software contours in the E_{total}-ΔE plane, like that shown in Fig. 1 for the 140-MeV spectrum. Also shown in Fig. 1 is the projected total-energy spectrum for all events within that contour. The counts in the lowest-energy channels in Fig. 1(d) to the left of the arrow comprise exclusively particles stopped in the ΔE detector and clearly include contributions from other than fusion processes, accounting for their sharp deviation from the smooth, broad, more-or-less symmetric peak shape expected for the lab energy distribution of all fusion products. The number of stopped fusion residues was taken as the area under the extrapolated portion of the smooth curve drawn through the data in Fig. 1(d). Similar extrapolations had to be made at all energies and angles; the resultant uncertainty assigned to the total fusion cross sections varies from ±1% at the highest energies to ±2% at 56 MeV.

Differential cross sections for the sum of all fusion products were measured at angles from $\theta_{lab} = 3°$ out to the maximum angle deemed necess-

ary to accurately determine the total cross section. Relative normalization of the yields at different angles was achieved by use of a Faraday cup beam integrator and of silicon surface-barrier monitor detectors placed symmetrically to the left (L) and right (R) of the incident beam direction, either at $\theta_{lab} = 10°$ in the scattering plane (at E_{lab} = 40, 45, 50, 75 MeV) or at a net angle of 15°, elevated 11° above the plane (at all other energies). For the measurements at LBL a third monitor detector was placed at 10° in the scattering plane to correct the $L+R$ sum for the sometimes large shifts in the vertical position of the beam on target, which were possible in the absence of entrance collimation in the scattering chamber. Changes in the L/R monitor ratio (or in-plane monitor-to-integrator ratio at LBL) were used to correct the fusion detector angle for horizontal beam displacements between runs. The absolute zero offset in the angle setting of the fusion telescope was determined at each energy by elastic-scattering measurements made with the telescope at nominally identical forward angles (3°–6°) to the left and right of the beam. With these procedures we were able typically to determine the detector angle to an accuracy of ±0.03°.

The fusion yields were corrected for dead time (≲15%) in the analog-to-digital conversion and computer processing of events. The raw detector counting rate was limited to a maximum of 3000/sec, and dead-time and pile-up losses in the remaining circuitry were found to be negligible.

The absolute normalization of fusion-detector yields was determined usually by setting the elastic-scattering cross sections measured at the most forward angles equal to the Rutherford values. At some energies this normalization procedure involved significant uncertainty, due either to uncertain subtraction of contaminant elastic yields (as at 40 and 45 MeV) or to insufficiently damped oscillations at the far forward angles in the elastic-scattering distribution (140 and 214 MeV). At these energies it was more accurate to simply adopt the same absolute normalization which had been determined from measurements at other energies using the same target and integrator, with appropriate corrections for the energy dependence of the mean charge state of the ^{16}O beam emerging from the target. The overall normalization uncertainty is estimated to be between ±2% and ±4%, depending on the bombarding energy.

The fusion angular distributions obtained at a number of bombarding energies are shown in Fig. 2. The total fusion cross sections were determined by angular integration of the smooth curves drawn through the measurements. As is clear from the insets in Fig. 2, the extrapolation of the differential cross section to 0° is quite well defined by the forward-angle data together with the requirement that $d\sigma/d\theta$ approach zero at 0°. The net uncertainty assigned to the total fusion cross section from the extrapolations to both small and large angles varies between ±0.5% and ±2%.

B. Remarks on the operational definition of the fusion cross section

The angular distributions in Fig. 2 are all strongly forward-peaked and appear to cut off sharply at angles ranging from 25° at the lowest

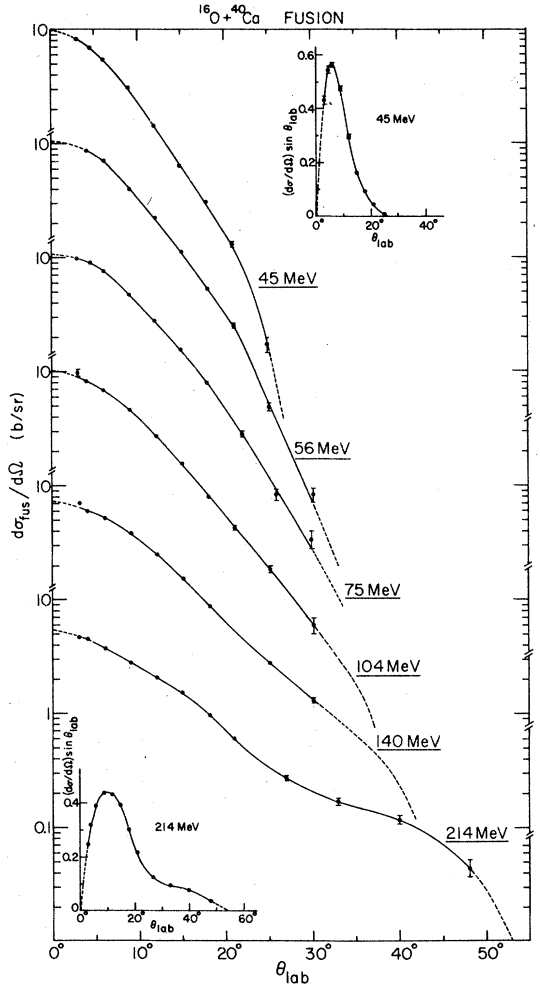

FIG. 2. Laboratory angular distributions of all fusion products at a number of bombarding energies. The total fusion cross sections are determined by integration of the smooth curves drawn through the measurements. The dashed portions of the curves indicate the assumed extrapolation of the differential cross section into unmeasured angular ranges. The insets show $(1/2\pi)\, d\sigma/d\theta$ at $E_{lab} = 45$ and 214 MeV.

energy to 50° at the highest. The cutoff angles are related to the maximum transverse recoil momentum which can be imparted to a fusion residue by the emitted particles. The gradual growth in extent of the angular distributions with increasing energy is interpreted as reflecting an increasing propensity for the composite nucleus to emit α particles or even larger clusters. Thus, the maximum angle at low energies is consistent with the emission of no more than one α particle, while at 214 MeV the emission of three energetic correlated α's (or of a ^{12}C nucleus) at angles near 90° in the compound-nucleus rest frame[35] would be required to account kinematically for the appreciable yield near $\theta_{lab} = 50°$.

This latter remark suggests that at least some of the "fusion products" at high bombarding energies result not from strict particle evaporation from an equilibrated compound nucleus, but rather from pre-equilibrium processes. Nonetheless, the observed concentration of the identified products in a fairly narrow region of Z above that of the target nucleus and their clear separation (even at 214 MeV) from other regions of *significant* reaction strength argue that in all cases their production is associated, by whatever detailed mechanism, with the formation of a long-lived composite system. It is our philosophy that a successful model should explain measurements of the "fusion" cross section defined *operationally* in the manner discussed here, which is common to most experiments. This operational definition is probably quite appropriate in discussing entrance-channel limitations on fusion, since in dynamical friction-model calculations[14,16-18,23] fusion reactions are generally identified simply as those for which the trajectories of the incident ions remain bounded after suitably long interaction times (i.e., a long-lived composite system is formed). The possibility that pre-equilibrium processes contribute to the measured cross sections must be kept in mind, however, in comparisons with predictions based on equilibrium properties of the compound nucleus.[20,21]

One further remark concerning our operational definition of fusion is in order. We have made no attempt to include fission products in the determined cross sections, although based on RLDM predictions (see Sec. IV B) one should expect substantial fission decay of the compound nucleus at the highest bombarding energies. Symmetric fission of the highly excited ^{56}Ni nuclei would produce fragments near Si, which are themselves probably at high temperature. These primary fragments would, in turn, decay by particle evaporation, leaving residues in the range from oxygen to aluminum.[5] A rough numerical estimate, made by blithely extrapolating fission-fragment kinetic energy systematics established for heavier systems at lower excitation,[36] suggests that at E_{lab} = 214 MeV one might expect residues at forward angles with lab energies between 50 and 100 MeV. A slight concentration of strength in the appropriate region of Z and E_{total} is perhaps discernible in Fig. 1(c), but a quantitative distinction between fission and deeply inelastic transfer strength in this region is not feasible with the available data.

C. Elastic-scattering measurements

The elastically scattered projectiles were detected and identified, along with inelastic and transfer reaction products, in a ΔE-E time-of-flight (TOF) telescope[37] for the 56- and 75-MeV measurements, and in simple three-counter telescopes at the higher energies (see Table I). The solid angles ranged from 0.02 to 0.2 msr, except for some extreme forward-angle measurements which were made at LBL using the fusion telescope, because of its smaller solid angle. Relative and absolute normalizations of the elastic cross sections were achieved by the same techniques as described above for the fusion data. In addition, yields obtained with the TOF telescope were corrected for losses from multiple scattering in the ΔE detector, as explained in Ref. 38.

The accurate determination of the scattering angle, corrected for any absolute zero offset and for beam displacements as in the fusion measurements, was crucial for establishing the correct shape of the elastic angular distribution at forward angles. This is especially true at 140 and 214 MeV, where the diffraction structure is still present at the most forward angles studied. At these energies the ratio of the elastic to Rutherford cross section ($\sigma_{el}/\sigma_{Ruth}$) was found to have a steep angular derivative at the monitor-detector angles, and consequently beam-shift corrections were made via an iterative procedure. In the first iteration, only the slope of the Rutherford cross section was used in translating observed changes in the L/R monitor ratio (or the in-plane monitor-to-integrator ratio) into actual beam displacements. The slope of $\sigma_{el}/\sigma_{Ruth}$ at the monitor angles, as determined from the first-iteration angular distribution, was included in deriving the second-iteration angle corrections. Corrections to the nominal telescope angle settings were sometimes as large as 0.4°.

Figure 3 displays a representative two-dimensional (E_{total} vs ΔE) spectrum acquired with the elastic telescope at 214 MeV. The spectrum clearly shows strength in lines corresponding to the elements B–Sc. The resolution in the projected total-energy spectra at all energies was sufficient

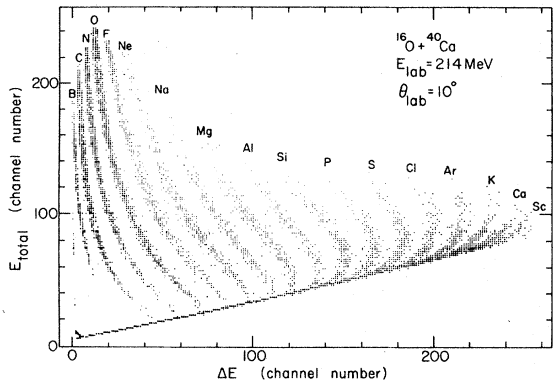

FIG. 3. Representative two-dimensional (E_{total} vs ΔE) spectrum acquired with the elastic telescope at $E_{\text{lab}}=214$ MeV. The lines corresponding to the various elemental products are labeled.

to resolve all inelastic reactions from the elastic-scattering peak. The inelastic-scattering and transfer reaction results at $E_{\text{lab}}=56$ and 75 MeV are reported elsewhere.[39,40]

III. RESULTS

The angular distributions for the elastic scattering of $^{16}O+^{40}Ca$ obtained in the present experiment are shown in Fig. 4. At each energy the measurements span at least two orders of magnitude in the ratio $\sigma_{el}/\sigma_{\text{Ruth}}$. The assigned errors include uncertainties associated with the following sources: (1) counting statistics, (2) determination of the scattering angle, (3) relative normalization via integrator and monitor-detector counts, (4) subtraction of contaminant yields, and (5) dead-time corrections. In general, contributions from one or both of the first two sources above are dominant. In addition, there is an overall normalization uncertainty between ±2% and ±4%, depending on the bombarding energy.

The curves displayed in Fig. 4 are fits to the measurements obtained in the optical model analysis, which will be discussed in Sec. IV D. The arrow associated with each angular distribution in Fig. 4 indicates the quarter-point angle ($\theta_{1/4}$), at which $\sigma_{el}/\sigma_{\text{Ruth}}=0.25$. Blair[41] has shown that in a simple strong absorption model the orbital angular momentum $l_{1/4}$ which is classically associated with Coulomb scattering to $\theta_{1/4}$ corresponds to the cutoff l value, below (above) which all partial waves lead to total (zero) absorption. The value of $\theta_{1/4}$ is thus useful for obtaining a purely empirical estimate of the total reaction cross section

$$\sigma_{\text{reac}} \simeq \pi\lambda\!\!\!^{-2} \sum_{l=0}^{l_{1/4}} (2l+1) \simeq \pi\lambda\!\!\!^{-2} l_{1/4}(l_{1/4}+1)\,, \qquad (1)$$

where

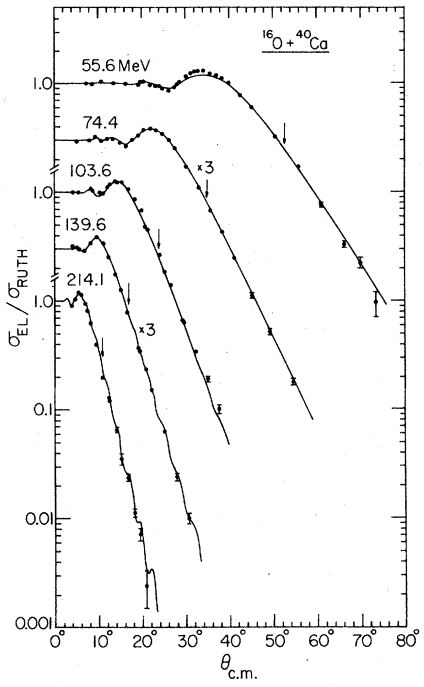

FIG. 4. Angular distributions for elastic scattering (ratio to Rutherford) of $^{16}O+^{40}Ca$ at five bombarding energies (specified in the figure). The solid curves represent an optical model fit to the data using the energy-independent potential 2a specified in Table IV. The arrows indicate angles where $\sigma_{el}/\sigma_{\text{Ruth}}=0.25$.

$$l_{1/4}=\eta\cot(\theta_{1/4}/2)\,, \qquad (2)$$

$\lambda\!\!\!^{-}$ is the entrance-channel de Broglie wavelength, η the Sommerfeld parameter, and it has been assumed that the barrier penetration coefficient $T_l=1$ for all $l \leq l_{1/4}$. [While strict evaluation of the summation in Eq. (1) would yield $(l_{1/4}+1)^2$, the form $l_{1/4}(l_{1/4}+1)$ is actually more appropriate in light of the replacement of the quantized angular momentum by a continuous classical variable.]

The measured total fusion cross sections are plotted as a function of $1/E_{\text{c.m.}}$ in Fig. 5. The error bars include contributions from the statistical uncertainty in the measured differential cross sections but are determined predominantly by the systematic errors discussed in Sec. II A, which arise in (1) defining the fusion region in the E_{total}-ΔE plane, (2) estimating the number of fusion residues stopped in the ΔE detector, (3) extrapolating the differential cross section to small and large angles, and (4) establishing the absolute cross section normalization. The various systematic errors have been combined linearly in estimating the overall error, which ranges from ±4% to ±9%. Also shown in Fig. 5 are the total reaction cross sections calculated using an energy-

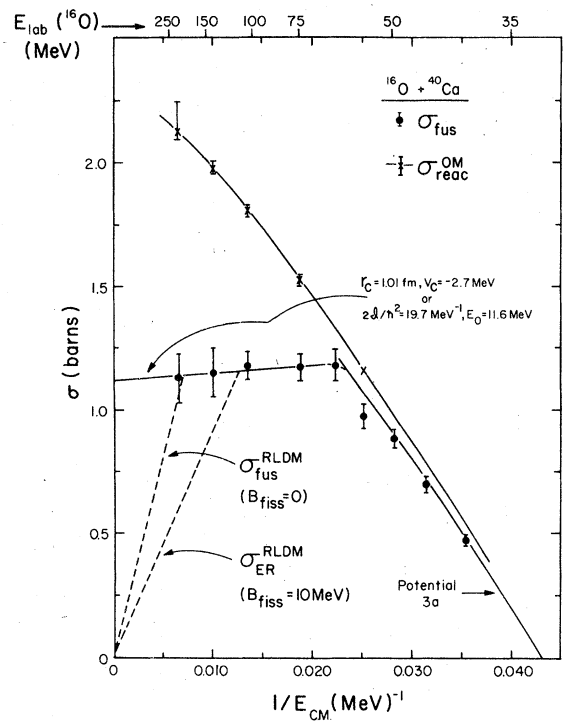

FIG. 5. Measured fusion (evaporation-residue) cross sections and optical model total reaction cross sections as a function of $1/E_{c.m.}$ The optical model results (both the crosses and the solid curve joining them) are for potential $2a$, with the size of the error bars indicating the spread in σ_{reac} values obtained using different potentials from Table IV. The solid-line fits to the fusion cross sections at high energy (using either the critical-distance or the yrast-limit models) and at low energy (using potential $3a$ from Table IV) are described in the text. The dashed lines indicate estimated upper limits on the total fusion (σ_{fus}) and evaporation-residue (σ_{ER}) cross sections based on the reduction and vanishing of the ^{56}Ni fission barrier predicted by the rotating-liquid-drop model (Ref. 21).

independent potential obtained in the optical model analysis (see Sec. IV D). The size of each error bar is an indication of the spread in σ_{reac} values predicted by different "best-fit" optical potentials. The curves in Fig. 5 will be discussed in Sec. IV.

The results in Fig. 5 present clear confirmation of the qualitative behavior which has been predicted for the fusion cross section by Glas and Mosel[3] and which has been observed experimentally in studies of lighter systems.[5-8] σ_{fus} exhausts most of σ_{reac} at low energies, but then breaks away from σ_{reac} abruptly at $E_{c.m.} \simeq 50$ MeV and remains roughly constant with further increase in bombarding energy. The fusion cross sections vary more or less linearly with $1/E_{c.m.}$, but with quite different slope and intercept parameters in the low- and high-energy regions.

The fusion and total reaction cross section data are summarized in Table II. The values of σ_{reac} calculated according to the quarter-point prescription of Eqs. (1) and (2) are specified for comparison with the optical model values. The agreement between the two values is good at all energies. It is also useful to compare $l_{1/4}$ to the limiting l value (l_{fus}) contributing to fusion in a sharp-cutoff expansion such as that of Eq. (1). It is clear from Table II that even above the "break" near $E_{c.m.} \simeq 50$ MeV, l_{fus} continues to increase with increasing energy, only much less rapidly than does $l_{1/4}$, reflecting the expanding band of high partial waves available for nonfusion reactions.

IV. DISCUSSION

A. Two simple models for the saturation of the fusion cross section

The various models which have been proposed to explain the energy dependence of fusion cross sections[1,3,12-20,33] are in basic agreement that at low energies the partial waves contributing to fusion are limited most severely by the requirement of surpassing the (nuclear + Coulomb + centrifugal) potential barrier. The abrupt "break" of σ_{fus} from σ_{reac} observed at higher energies in the present and in previous[5-8] experiments signifies that this "barrier penetration" condition is no longer sufficient to ensure fusion. The low-energy fusion data will be discussed and the "barrier penetration" condition clarified in Sec. IV E. In the present section we extract the parameters necessary to fit the high-energy ^{16}O + ^{40}Ca measurements in two simple models, which are representative of the two classes of fusion models described in Sec. I. Other possible models will be considered qualitatively in Sec. IV C.

The first model to be discussed here attributes the limitation on high-energy fusion to the requirement that the colliding ions penetrate to a certain critical separation (R_c), where dissipation of the relative kinetic energy into internal excitation sets in rapidly.[3,13-15] (At low energies this separation is reached whenever the outer potential barrier is surpassed.) Glas and Mosel[13,14] argue that this abrupt onset of friction is a result of the shell structure of the colliding nuclei and is to be associated with the onset of level crossings in a two-center shell-model picture of the composite system. In the second model the restriction on fusion is related to the limiting (yrast) angular momentum for the compound-nucleus states at a given excitation.[4,6,7] The predictions of both models are most easily expressed in a sharp-cutoff approximation, in which all partial waves up to and including l_{fus} are assumed to have unit prob-

TABLE II. The measured fusion and calculated total reaction cross sections as a function of bombarding energy.

E_{lab} (MeV)	E^* (^{56}Ni) [a] (MeV)	$1/E_{c.m.}$ (MeV)$^{-1}$	σ_{fus} (mb)	l_{fus} [b]	$l_{1/4}$ [c]	$\sigma_{reac}^{1/4}$ [d] (mb)	σ_{reac}^{om} [e] (mb)
39.6	42.6	0.035 4	471 ± 25	14.7 ± 0.4			535
44.6	46.2	0.031 4	696 ± 32	19.1 ± 0.5			784
49.7	49.8	0.028 2	884 ± 35	22.9 ± 0.5			981
55.6	54.0	0.025 2	974 ± 50	25.4 ± 0.7	27.6 ± 0.1	1142 ± 10	1162
62.7	59.1	0.022 3	1182 ± 65	29.8 ± 0.8			1328
74.4	67.4	0.018 8	1172 ± 53	32.4 ± 0.7	36.8 ± 0.2	1508 ± 19	1529
103.6	88.3	0.013 5	1179 ± 55	38.5 ± 0.9	46.8 ± 0.3	1736 ± 22	1812
139.6	114.0	0.010 0	1153 ± 100	44.2 ± 1.9	57.4 ± 0.4	1931 ± 23	1981
214.1	167.2	0.006 54	1127 ± 100	54.3 ± 2.4	73.9 ± 0.7	2078 ± 39	2123

[a] Excitation energy in the compound nucleus.
[b] Determined from the measured σ_{fus} via Eq. (3).
[c] Determined from the measured elastic-scattering quarter-point angle ($\theta_{1/4}$) via Eq. (2). $\theta_{1/4}$ is determined from an exponential fit to the data (averaging over oscillations) in the Coulomb rainbow region. The errors quoted correspond to an uncertainty of ±4% in the value of σ/σ_{Ruth} near $\theta_{1/4}$.
[d] Determined via Eq. (1).
[e] Calculated using the energy-independent optical model potential 2a in Table IV. Other potentials which also fit the elastic-scattering data generally yield σ_{reac} values within ±2.5% of these (not including the absolute normalization uncertainty in the measurements).

ability of penetrating the potential barrier ($T_l = 1$) and of leading to fusion ($P_l = 1$), while for all higher partial waves $T_l P_l = 0$. Thus

$$\sigma_{fus} = \pi \lambda\!\!\!^{-2} l_{fus}(l_{fus}+1), \tag{3}$$

and the problem is reduced to determining l_{fus}.

In the critical-distance (CD) model l_{fus} is taken to be that partial wave which has its classical turning point at $r = R_c$:

$$E_{c.m.} = V_c + \frac{l_{fus}(l_{fus}+1)\hbar^2}{2\mu R_c^2}, \tag{4}$$

where V_c is the value of the $l=0$ (nuclear + Coulomb) potential at R_c and μ is the entrance-channel reduced mass. Assuming R_c to be constant, independent of energy, we get from Eqs. (3) and (4):

$$\sigma_{fus} = \pi R_c^2 \{1 - V_c/E_{c.m.}\}. \tag{5}$$

A similar expression results from the yrast-limit (YL) model if we associate l_{fus} with a parabolic compound-nucleus yrast line:

$$E^* = E_{c.m.} + Q_{fus} = \frac{\hbar^2}{2\mathcal{I}} l_{fus}(l_{fus}+1) + E_0, \tag{6}$$

giving

$$\sigma_{fus} = \pi \frac{\mathcal{I}}{\mu}\{1 + (Q_{fus} - E_0)/E_{c.m.}\}. \tag{7}$$

In Eqs. (6) and (7), E^* is the excitation energy at which the compound nucleus is formed, Q_{fus} is the ground-state Q value for the fusion reaction, and $\mathcal{I}$ the moment of inertia characterizing the yrast band whose spin-zero state would lie at excitation energy E_0.

Equations (5) and (7) are both capable of fitting the observed energy dependence of high-energy fusion cross sections for any one system with reasonable values of the parameters R_c, V_c, or $\mathcal{I}$, E_0. Indeed the predictions are identical under the conditions

$$\mathcal{I} = \mu R_c^2 \tag{8}$$

and

$$V_c = E_0 - Q_{fus}. \tag{9}$$

(Some relationship between V_c and $-Q_{fus}$ is even *expected* for an adiabatic nucleus-nucleus potential,[29,42] whose application at R_c is consistent with the neglect in the CD model of all dissipative processes at $r > R_c$.) The equivalence between the predictions of the two models is expected to break down when we consider several entrance channels to the same compound nucleus, which should all be characterized by the same values of $\mathcal{I}$ and E_0 but not, in general, of μR_c^2 and $(V_c + Q_{fus})$. If, for example, we assume that

$$R_c = r_c(A_1^{1/3} + A_2^{1/3}), \tag{10}$$

with the value of r_c roughly independent of the masses A_1, A_2 of the colliding nuclei,[1-3] then μR_c^2 decreases rapidly with increasing mass asymmetry $\{|A_2 - A_1|/(A_1 + A_2)\}$ of the entrance channel, and the equality (8) cannot be maintained. The two models can then be distinguished by the behavior of the extrapolated asymptotic ($1/E_{c.m.} \to 0$) fusion cross section as a function of the entrance-channel mass asymmetry for a given compound nucleus. Appropriate data are not yet available for light

TABLE III. Model parameters [a] extracted from fits to high-energy fusion cross sections for various light systems.

Entrance channel	Compound nucleus	Ref.	Critical-distance model V_c (MeV)	R_c (fm)	$R_c/(C_1+C_2)$ [b]	Yrast-limit model E_0 (MeV)	$2\mathcal{I}/\hbar^2$ $(\text{MeV})^{-1}$	$\mathcal{I}/\mathcal{I}_{rs}$ [c]
$^{12}C+^{12}C$	^{24}Mg	5	−14 ± 9.0	4.3 ± 0.50	0.96 ± 0.11	−0.1 ± 9.0	5.3 ± 1.2	0.75 ± 0.17
$^{14}N+^{12}C$	^{26}Al	7,48	−0.4 ± 3.0	5.45 ± 0.35	1.17 ± 0.08	14.7 ± 3.0	9.2 ± 1.2	1.19 ± 0.15
$^{16}O+^{12}C$	^{28}Si	5	−5.5 ± 6.5	4.9 ± 0.65	1.01 ± 0.13	11.3 ± 6.5	7.9 ± 2.1	0.92 ± 0.24
$^{18}O+^{12}C$	^{30}Si	5	−9.2 ± 6.0	5.2 ± 0.45	1.05 ± 0.09	14.4 ± 6.0	9.3 ± 1.6	0.99 ± 0.17
$^{12}C+^{27}Al$	^{39}K	4,8	−12 ± 10	5.35 ± 0.35	1.03 ± 0.07	4.6 ± 10	11.4 ± 1.5	0.79 ± 0.10
$^{16}O+^{40}Ca$	^{56}Ni	present work	−2.7 ± 8.5	6.00 ± 0.40	0.97 ± 0.06	11.6 ± 8.5	19.7 ± 2.6	0.78 ± 0.10
$^{40}Ca+^{40}Ca$	^{80}Zr	d	22 ± 17	6.7 ± 1.0	0.95 ± 0.14	e	43.0 ± 12.8	e

[a] The quoted uncertainties reflect a subjective judgement on the range of acceptable fits to each data set, keeping in mind that the measurement errors are in all cases predominantly systematic.

[b] The half-density radii C_1 and C_2 for the entrance-channel nuclei have been estimated from electron-scattering results, by averaging the various values tabulated for each nucleus in Ref. 43.

[c] The rigid-sphere moment of inertia $\mathcal{I}_{rs}$ is calculated from Eq. (11), using mean-squared charge radii averaged over the various values tabulated in Ref. 43. In cases where electron-scattering data are not available, $\langle r_{cn}^2\rangle$ has been estimated from results for nearby nuclei.

[d] H. Doubre, A. Gamp, J. C. Jacmart, N. Poffé, J. C. Roynette, and J. Wilczynski, Phys. Lett. 73B, 135 (1978).

[e] Parameter values not specified due to lack of information about the mass and density distribution of the compound nucleus.

systems.

The straight-line fit to the high-energy data in Fig. 5 results from Eq. (5) with parameter values $R_c = 6.00$ fm ($r_c = 1.01$ fm) and $V_c = -2.7$ MeV or from Eq. (7) with parameter values $2\mathcal{I}/\hbar^2 = 19.7$ MeV^{-1} and $E_0 = 11.6$ MeV. These values are compared in Table III with those necessary to fit the high-energy fusion data for some representative light systems. The uncertainties quoted in Table III reflect the range of parameter values with which acceptable fits can be obtained subject to readjustment of the other parameter; they are especially large for the oscillatory fusion excitation functions observed[5] for $^{12}C+^{12}C$ and $^{16}O+^{12}C$, where one can attempt to fit only the average energy dependence with Eqs. (5) or (7). For each system in Table III we also compare the extracted critical radius to the sum (C_1+C_2) of the half-density radii of projectile and target nuclei, and the moment of inertia $\mathcal{I}$ to the value for a rigidly rotating spherical compound nucleus of mass A_{cn} and mean-squared matter radius $\langle r_{cn}^2\rangle$:

$$\mathcal{I}_{rs} = \tfrac{2}{3} A_{cn} \langle r_{cn}^2 \rangle . \qquad (11)$$

The matter-density distribution parameters C_1, C_2, and $\langle r_{cn}^2\rangle$ were estimated from electron-scattering results.[43]

It is clear from Table III that most high-energy fusion cross sections measured to date can be fitted reasonably well with $R_c \simeq C_1 + C_2$ or $\mathcal{I} \simeq (0.9)\mathcal{I}_{rs}$: possible deviations from this simple behavior[5,13] for tightly bound colliding nuclei ($^{12}C+^{12}C$, $^{16}O+^{12}C$, $^{16}O+^{40}Ca$, $^{40}Ca+^{40}Ca$) are masked by experimental uncertainties. Effects of the shell structure of the target and projectile nuclei may be more clearly visible in the behavior of the observed maximum fusion cross section (σ_{fus}^{max}) than in any of these model parameters.[5,31] The value of σ_{fus}^{max} (= 1180 mb) for $^{16}O+^{40}Ca$ is quite consistent with the observations for other systems involving one p-shell nucleus and one sd-shell nucleus.[5,31]

Some insight into the relative validity of the YL and CD models can be gained by comparing the parameters necessary to fit the present fusion data with theoretical predictions of the compound-nucleus yrast line or of the nucleus-nucleus potential. This is done in Secs. IV B and IV E, respectively.

B. Comparison with predictions of the rotating-liquid-drop model

The yrast line which would be defined by the $^{16}O+^{40}Ca$ fusion data in the YL model is compared with that predicted by the rotating-liquid-drop model[21] (RLDM) in Fig. 6. For each bombarding energy included in the plot, the fusion cross section is represented by a solid line at a constant value of the compound-nucleus excitation energy E^*, indicating the range of partial waves contributing to σ_{fus} in the sharp-cutoff approximation of Eq. (3). The l values between l_{fus} and $l_{1/4}$ of Eq. (2), which account in this simple picture for all the nonfusion reaction cross sections, are indicated by the dashed extension to each line. The parabolic yrast line corresponding to the parameters $\mathcal{I}$, E_0 specified in Table III would connect the end points of the solid lines drawn for

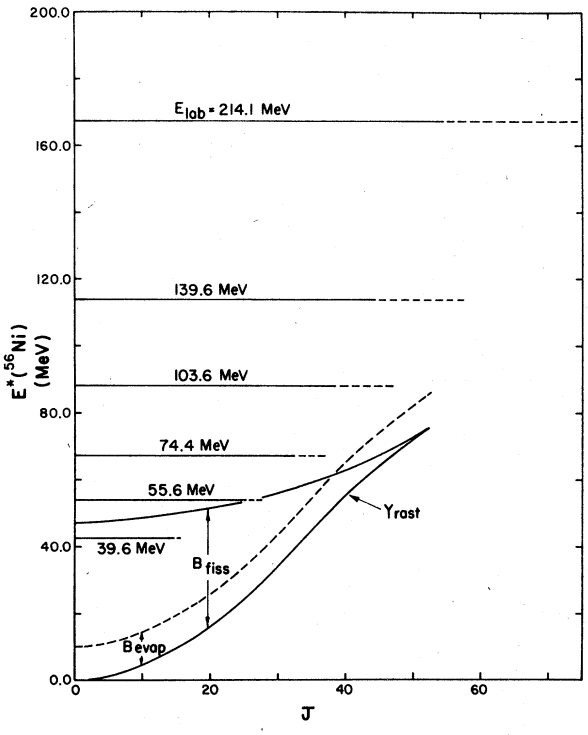

FIG. 6. The range of angular momenta contributing in a sharp-cutoff approximation to the measured fusion (solid lines) and total reaction (dashed lines) cross sections, plotted for several compound-nucleus excitation energies. The curves representing the yrast line and particle evaporation and fission thresholds for ^{56}Ni as a function of spin are based on the rotating-liquid-drop model (Ref. 21).

$E_{lab} \geq 75$ MeV. The RLDM yrast line, deduced from graphs in Ref. 21, maps out the minimum total (surface + Coulomb + rotational) energy calculated for a rigidly rotating, charged, deformable liquid drop representative of ^{56}Ni.

The very poor agreement apparent in Fig. 6 between the "empirical" and RLDM yrast lines is evidence against the validity of the simple YL model. The sharp-cutoff approximation we have used in this model might lead naturally to an underestimate of the yrast spin at each excitation, because in reality the density of states, and hence the fusion probability P_l, will fall off smoothly (rather than abruptly) toward zero at the yrast spin; however, this effect cannot be large enough to account for the observed discrepancies in Fig. 6. The inclusion of shell corrections may be expected to modify the predicted yrast energies significantly[44,45] but, again, not so grossly as the fusion data would require. In terms of the parameters of Eq. (7) the deviation from RLDM calculations shows up most clearly in the value of $\mathcal{I}$: In the relevant region of spin the liquid drop is predicted[21] to pass from a mildly deformed oblate shape to a "super-deformed" triaxial shape, characterized by a moment of inertia roughly twice as large as that for a rigid sphere ($\mathcal{I}_{rs}$), in marked contrast to the YL-model value of $0.78\mathcal{I}_{rs}$.

Also plotted as a function of spin in Fig. 6 are the excitation energies required for fission of the rotating liquid drop[21] and for evaporation of a typical particle from nuclides near ^{56}Ni. For the purposes of a qualitative discussion, we have assumed a spin-independent particle evaporation barrier (B_e) of 10 MeV, whereas the actual energy required to remove a neutron, proton, or α particle (and overcome the Coulomb barrier) from a spherical ^{56}Ni nucleus is approximately 17, 12, or 17 MeV, respectively. Throughout much of the region of super-deformed yrast shapes, the fission barrier $B_f < B_e$. Consequently, we should expect appreciable probability for fission decay of the high-spin compound nuclei formed in $^{16}O + ^{40}Ca$ collisions at $E_{lab} = 140$ and 214 MeV. As pointed out in Sec. II B, the present data do not rule out the occurrence of non-negligible fission cross sections, but we have made no attempt to include fission products in evaluating σ_{fus}.

The RLDM fission barrier for ^{56}Ni vanishes at a critical angular momentum $J_{cr} = 52.5$. Regardless of the mechanism limiting σ_{fus} in the saturation region we have been discussing, it has been widely presumed[21,46,47] that partial waves above J_{cr} cannot contribute to fusion, since no equilibrium compound-nucleus states of appropriate spin exist. Such a fixed upper partial-wave limit yields σ_{fus} values [see Eq. (3)] which fall toward zero proportionately to $1/E_{c.m.}$, as illustrated by the upper dashed line in Fig. 5. While the $^{16}O + ^{40}Ca$ fusion measurement at $E_{lab} = 214$ MeV is not inconsistent with the RLDM upper limit on the total fusion cross section, it *is* inconsistent with the corresponding limit on the *evaporation-residue* cross section, as represented by the lower dashed line in Fig. 5. This lower dashed line is intended only as a qualitative estimate, based on the crude assumption that the compound nucleus decays exclusively via fission when $B_f \leq 10$ MeV and via particle evaporation when $B_f > 10$ MeV. Measurements for several other systems[6,8,47] suggest similar possible violations of the RLDM prediction[21] of a dramatic turnover in σ_{fus} ($E_{c.m.}$) as $B_f \to 0$, but in all these cases no firm conclusion can be reached without data at still higher energies. On the other hand, recent fusion data for $^{14}N + ^{12}C$ seem to indicate a high-energy falloff *consistent* with RLDM expectations.[31,48]

In light of the conclusion from Fig. 6 that ^{56}Ni is populated at high temperature even for the highest spins studied, it should not be very surprising if the fission barrier of the "cold" compound nucleus

has little relevance to the $^{16}O+^{40}Ca$ evaporation-residue cross section. At high temperature a sizable fraction of the total angular momentum and excitation energy may arise from single-particle, as opposed to collective, motion[47] and may be most easily removed from the composite system by the pre-equilibrium emission of energetic light particles. The ultimate decay mode of the composite system might then be governed by the yrast line and fission barrier in the cooled residues of the pre-equilibrium stage, which have slightly lower mass and considerably lower spin than the initially formed $^{56}Ni^*$. Recent gamma-multiplicity measurements for light systems[49,50] confirm that considerable angular momentum is carried off by emitted particles prior to the yrast γ cascade in the "evaporation" residues. Furthermore, there is evidence in the present data for the emission of energetic α particles accompanying $^{16}O+^{40}Ca$ fusion at the highest energies studied (see Sec. II B), although it is not clear whether these particles originate mainly from collisions with high or with low impact parameter. (It is plausible, for example, that such α particles would be preferentially formed in and ejected from the regions of highest density and temperature, which occur in head-on collisions.)

It is clear from the above discussion that the magnitude of the measured evaporation-residue cross section at $E_{lab}=214$ MeV does not *necessarily* imply that the high-spin fission barrier for ^{56}Ni is underestimated by the RLDM. It is intriguing nonetheless to note that Neergard *et al.*[44] predict that shell corrections should quite generally lead to an increase in J_{cr} over the RLDM value.

C. Comments on the nature of the physical limitation to high-energy fusion

The comparison with RLDM predictions suggests that the simple compound-nucleus yrast limitation to high-energy fusion is not applicable for the present system. It is important to point out that the alternative critical-distance model also has shortcomings. Most significant is the conceptual problem posed by the complete neglect of all flux, energy, and angular momentum dissipation at separations $r>R_c$. The model in its simplest form is thus unable to account for the substantial damping observed[8,9] in the fusion saturation energy region for *nonfusion* products, which are most naturally associated with those partial waves which surpass the outer potential barrier but do not quite reach R_c [a situation depicted at the energy E_2 in Fig. 7(a)]. For light systems, such as $^{16}O+^{40}Ca$, where the transfer products are seldom *completely* damped, the situation might be improved without *seriously* distorting the predicted fusion energy dependence by including in the model a *weak* frictional force for $r>R_c$. Even weak friction in this region, however, is likely to destroy the simple linear relationship between σ_{fus} and $1/E_{c.m.}$ [Eq. (5)], since high partial waves with turning points well outside R_c, but for which $E_{c.m.}$ barely exceeds the potential barrier height, will begin to get "trapped" in the potential well and contribute to fusion[16] [see dashed curves in Fig. 7(a)]. The parameters R_c, V_c extracted from straight-line fits to high-energy fusion data would then provide at best *qualitative* information on the depth of the nucleus-nucleus potential.

Several alternative mechanisms for the saturation of the fusion cross section at high energies have been proposed and are worthy of mention. Relevant features of each of these mechanisms are summarized schematically, along with the critical-distance model, in Fig. 7. For the reasons discussed below, none of these other mechanisms would appear to be dominant for light systems.

In the strong friction limit discussed in Refs. 16–18 and illustrated in Fig. 7(b), surpassing the outer barrier of the conservative potential continues to be a sufficient condition for fusion at high energies, just as it is at lower energies. Since the barrier moves to progressively smaller radii with increasing angular momentum, one expects that as the bombarding energy is raised, more energy will be dissipated in the surface region outside the barrier for the near-grazing l's, and consequently an expanding band of high partial waves will be *removed* from the fusion channel. The effect would be a gradually increasing deviation between σ_{fus} and σ_{reac}. It seems unlikely that the *abrupt* break between σ_{fus} and σ_{reac} observed in Fig. 5 could be explained without introducing some mechanism for producing a similarly abrupt increase in the strength of the surface friction. Moreover, the assumption that strong surface friction is responsible for the saturation of σ_{fus} in collisions of light nuclei seems inconsistent with the fusion excitation functions measured[5] for $^{12}C+^{12}C$ and $^{16}O+^{12}C$, which exhibit oscillations superimposed on an average energy dependence similar to that in Fig. 5. Although the origin of these oscillations is not understood in detail, they most likely reflect particularly *weak* absorption (and hence friction) in the region of the potential well.[5]

Another possibility is that the l values contributing to fusion are limited by the disappearance of a "pocket" in the entrance-channel potential.[1,11,15,19] In its simplest form this model would yield a fixed value of l_{fus} at energies above the "bend" in σ_{fus} ($E_{c.m.}$), in disagreement with measurements (e.g., see Table II). This objection can be removed by

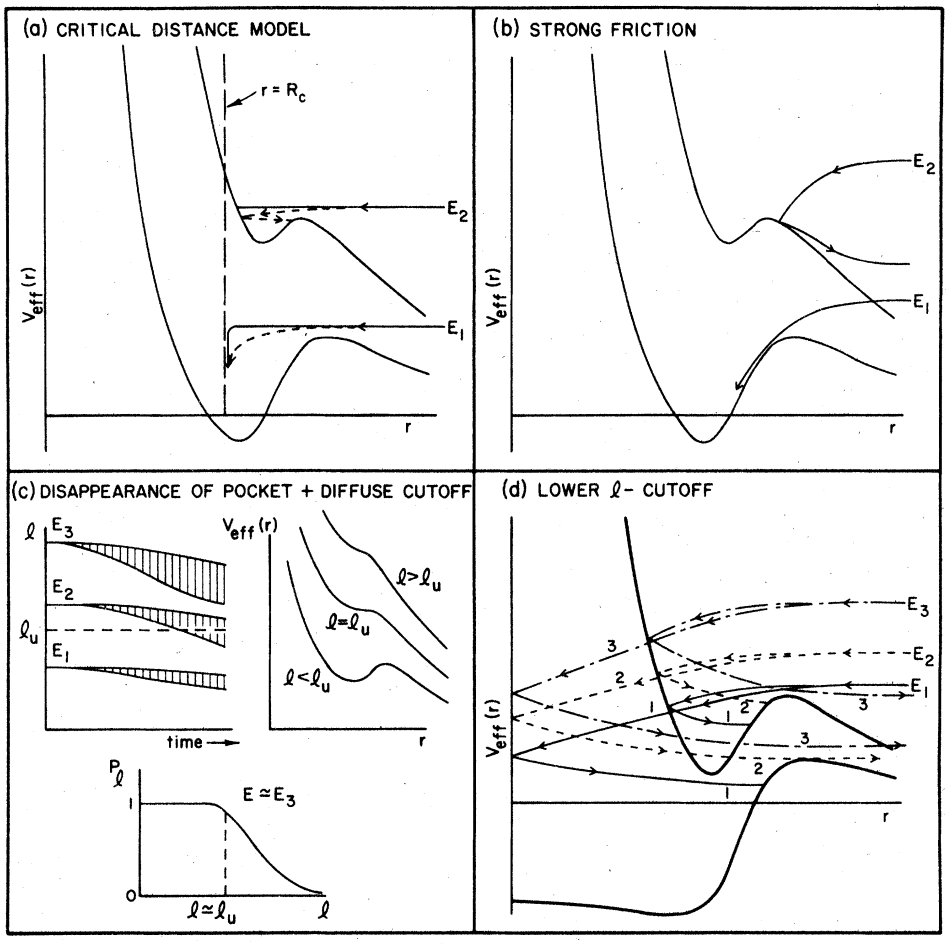

FIG. 7. Schematic illustration of several different possible mechanisms for the saturation of high-energy fusion cross sections. (a) In the critical distance model, surpassing the outer potential barrier is sufficient at low energies (E_1) and low l, but not at high energies (E_2) and high l, to ensure penetration to R_c and fusion. The dashed curves indicate the effect of adding to the model a weak radial friction force at $r > R_c$. (b) In the strong friction limit, energy dissipation outside the potential barrier increases in importance with increasing energy and removes a progressively widening band of suborbiting partial waves from the fusion channel. (c) The plot of l vs time indicates the qualitative effect of angular momentum dissipation on a representative subgrazing partial wave at each of three energies. The band of statistically distributed post-friction relative angular momenta (shaded areas) overlaps completely (E_1), partially (E_2), or not at all (E_3), with the range of $l(\leq l_u)$ in which the conservative potential $V_{\text{eff}}(r)$ exhibits a pocket. The result is a diffuse cutoff in the fusion probability coefficients P_l. (d) At energy E_1 frictional losses are sufficient to yield "trapping" in the potential pockets (and hence, fusion) for both partial waves depicted. At E_2 fusion occurs only for the upper of the two partial waves, and at E_3 it occurs only for the upper of the two partial waves, and at E_3 it occurs for neither. The fusion cross section thus saturates above E_2 as a result of the increasing lower l cutoff.

assuming a smooth transition, rather than a sharp cutoff, in the fusion probability from $P_l = 1$ to $P_l = 0$. Such a smooth transition might arise, for example, from angular momentum dissipation,[19,51] as a result of which each asymptotic partial wave l_a will give rise in the interaction region to a statistical distribution of lower partial waves [as indicated by the shaded regions in Fig. 7(c)]. This distribution may partially overlap with the range of l values ($l \leq l_u$) for which the effective real potential exhibits a pocket, even if $l_a > l_u$, in which case $0 < P_{l_a} < 1$. We may then expect the fusion cross section to saturate at energies [e.g., E_2 in Fig. 7(c)] for which l values above l_u first become available for reactions. But we must also expect a higher-energy falloff (characteristic of a fixed value of l_{fus}) when the near-grazing partial waves begin to exceed l_u by a larger margin than can be easily dissipated [as is the case for E_3 in Fig. 7(c)]. A reasonable estimate of the *maximum* probable angular momentum dissipation is provided by the "sticking" limit,[15,52] in which the two frag-

ments undergo intrinsic rotations with equal angular velocities, and the post-friction relative angular momentum l_s is reduced to

$$l_s = l_a\left(1+\frac{2}{5}\frac{M_1C_1^2+M_2C_2^2}{\mu(C_1+C_2)^2}\right)^{-1}; \quad (12)$$

in Eq. (12), M_1 and M_2 are the masses, C_1 and C_2 the half-density matter radii, and μ the reduced mass of the colliding nuclei. Applying these concepts to $^{16}O+^{40}Ca$, the observed onset of saturation in σ_{fus} at $E_{c.m.}\simeq 50$ MeV implies $l_u \simeq 33$; since $l_s \simeq 33$ when $l_a \simeq 52$, the high-energy falloff should begin when $l_{1/4}\simeq 52$ or $E_{c.m.}\simeq 83$ MeV; such a falloff is not observed in Fig. 5. This model is thus not capable of accounting quantitatively for the observed *extent* of the fusion saturation energy region. (A similar difficulty is found with the global semiempirical parametrization of heavy-ion fusion cross sections recently proposed by Horn and Ferguson[53]: Their prescription provides good quantitative agreement with the present low-energy data and the observed bend at $E_{c.m.}\simeq 50$ MeV but yields a higher-energy turnover not observed in the measurements.)

Two additional models for the limitation on high-energy fusion have implications for the distribution of *nonfusion* reaction strength which are inconsistent with the charged-particle spectra observed for $^{16}O+^{40}Ca$ and comparable systems. The first of these attributes the saturation of σ_{fus} to a *lower* l cutoff which increases with increasing energy and which arises because the energy dissipation is insufficient at high energies to yield "trapping" in the potential pockets for the lowest partial waves [see Fig. 7(d)]. In head-on collisions the nuclei would then "pass through" one another, emerging with their relative kinetic energy essentially totally dissipated. Such an effect is indeed predicted by dynamical calculations based on both macroscopic[18,52] and microscopic[54] treatments of friction, as well as by time-dependent Hartree-Fock calculations (the "vibrational instability" discussed in Ref. 22). In such a model one would expect the "missing" fusion strength to appear in very strongly damped reaction products completely separated from the quasielastic strength.[22,54] This separation should be most pronounced at energies just above the "bend" in σ_{fus} $(E_{c.m.})$ [e.g., just above E_2 in Fig. 7(d)], where the low l products would emerge with energies at best barely exceeding the exit-channel Coulomb ($l=0$) barrier. The *observed* cross section[40] for such low-energy nonfusion products from $^{16}O+^{40}Ca$ at $E_{lab}=75$ MeV falls far short of that needed to explain the reduced fusion, and it is thus unlikely that a lower l cutoff could be a dominant cause for the saturation of σ_{fus} in this system. Also, since most of the "missing" fusion strength for $^{16}O+^{40}Ca$ appears in C, N, and O isotopes (see Fig. 1) which cannot be construed as fission products, the argument[20] that the evaporation-residue cross section saturates as a result of fission competition does not seem applicable.

In conclusion, none of the models considered above is completely satisfactory, but the critical-distance limitation to high-energy fusion, with some account taken of weak dissipative effects at $r>R_c$, is probably the most appropriate for light systems. Several of the other mechanisms discussed may play a more relevant role in much heavier systems, where, however, the application of a simple one-dimensional potential model is more questionable.[55]

D. Optical model analysis of the elastic-scattering data

A conventional optical model analysis of the $^{16}O+^{40}Ca$ elastic-scattering data has been carried out using the code PTOLEMY.[56] The potentials employed consisted of a real central well and a volume imaginary term, both of Woods-Saxon shape. Three different search procedures were used, and representative potentials obtained with each are specified in Table IV. In the first procedure, four of the six potential parameters (usually the real well and imaginary well geometry parameters) were adjusted to fit the angular distributions at each bombarding energy *individually*. As is typical for strongly absorbed projectiles,[57,58] equally good fits to the data at each energy were obtained with a wide variety of potentials. The relationships among the various best-fit potentials will be discussed below. In the second procedure, four parameters of an *energy-independent* potential were varied to fit the data at all energies *simultaneously*. Although the potential ambiguities were not explored as thoroughly as in the individual-energy analyses, it is clear again that a number of equivalent potentials can be found. The curves in Fig. 4 and the σ_{reac} values plotted in Fig. 5 were calculated with a potential ($2a$ in Table IV) obtained via this procedure. In the third procedure, fits to all the elastic data were obtained using a single energy-independent *real* potential and adjusting the three parameters of the imaginary term independently at each energy. The parameters of the real potential were held fixed at values which provided an optimum simultaneous fit to the 56-MeV elastic-scattering data and to the low-energy fusion data, as described in the following subsection. The potentials obtained in this procedure still provide an acceptable fit to the elastic data at 75 MeV, but the quality of fit deteriorates significantly at the higher energies (see χ^2 values in Table IV).

TABLE IV. Optical model parameters for representative best-fit Woods-Saxon potentials.[a]

E_{lab} (MeV)	Potential label	V_0 (MeV)	r_R[b] (fm)	a_R (fm)	W (MeV)	r_I[b] (fm)	a_I (fm)	χ^2 per degree of freedom
				Procedure 1				
55.6	1*a*1	100.0	1.309	0.403	24.0	1.397	0.173	3.53
55.6	1*a*2	10.0	1.526	0.300	20.0	1.460	0.125	3.57
74.4	1*b*1	100.0	1.110	0.629	24.0	1.247	0.510	1.52
74.4	1*b*2	10.0	1.448	0.452	20.0	1.361	0.340	0.70
103.6	1*c*1	100.0	1.109	0.602	24.0	1.218	0.562	3.71
103.6	1*c*2	10.0	1.419	0.406	20.0	1.264	0.523	3.46
139.6	1*d*1	100.0	1.002	0.765	24.0	1.238	0.547	2.81
139.6	1*d*2	10.0	1.375	0.600	20.0	1.295	0.492	1.85
214.1	1*e*1	100.0	1.034	0.719	24.0	1.236	0.618	2.05
214.1	1*e*2	10.0	1.386	0.485	20.0	1.260	0.646	4.57
				Procedure 2				
All	2*a*	10.0	1.379	0.605	20.0	1.304	0.483	4.81[c]
All	2*b*	100.0	1.017	0.749	24.0	1.247	0.538	5.33[c]
				Procedure 3				
55.6	3*a*	27.97	1.329	0.50	6.41	1.230	0.115	3.28
74.4	3*b*	27.97	1.329	0.50	101.6	1.197	0.403	1.77
103.6	3*c*	27.97	1.329	0.50	90.96	1.280	0.277	14.2
139.6	3*d*	27.97	1.329	0.50	123.7	1.069	0.673	38.5
214.1	3*e*	27.97	1.329	0.50	20.93	1.308	0.757	15.6

[a] The three search procedures are described in Sec. IV D of the text. Variables held fixed during searches are indicated for each set listed by underlines.

[b] The radius parameters are to be multiplied by $(A_1^{1/3}+A_2^{1/3})$. The Coulomb radius parameter was held fixed for all potentials at 1.25 fm.

[c] The net χ^2 values for the simultaneous fit to the data at *all* energies are specified for procedure 2.

The various real potentials which provide equivalent fits to the measurements at each energy (in the first procedure above) are related to each other in some cases by the Igo ambiguity,[59] nearly coinciding throughout the surface region. In other cases, the "equivalent" real potentials are characterized by significantly different values of the diffuseness, but they are found to have roughly similar depths in a small radial region centered about a radius R_x, which varies with energy between 9 and 10 fm. The occurrence of a "crossover" among various best-fit real potentials has been noted in a number of previous analyses of heavy-ion elastic scattering.[57,58,60-63] In contrast to these earlier results, we find in the present analysis that *no unique, sharp crossover point is defined* unless one arbitrarily confines consideration to some subset of all the potentials which provide fits of equivalent quality to the data.

The latter point is illustrated in Fig. 8, where we have plotted the tail region of the real potentials belonging to two different "families," with depths $V_0 \simeq 10$ MeV and $V_0 \simeq 25$ MeV, respectively. The potentials within each family have been gen-

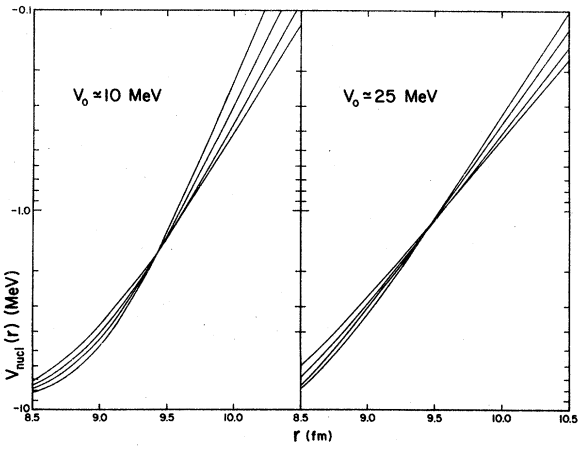

FIG. 8. The tail region of the real central wells for various best-fit potentials obtained in the optical model analysis of the 56-MeV elastic-scattering data. Note that the two potential families, corresponding to $V_0 \simeq 10$ MeV and $V_0 \simeq 25$ MeV, respectively, define different crossover points.

erated by changing the real well diffuseness a_R in discrete steps and then readjusting the remaining five parameters, from fixed starting values, for an optimum fit to the 56-MeV elastic-scattering data. The potentials included in Fig. 8 all yield values of χ^2 per degree of freedom ≤ 3.0. (The variation of χ^2 with a_R for each family is plotted in Fig. 12 and will be discussed later.) It is clear that the potentials within each family do define a sharp crossover point, in each case at $r \simeq 9.4$ fm, but the two crossovers differ significantly from one another [$V(r) = -1.75$ MeV for the 10-MeV deep potentials, $V(r) = -1.35$ MeV for the 25-MeV deep potentials]. When one includes potentials from a number of such families, the closest approach to an overall crossover for 56 MeV occurs at $R_x \simeq 9.7$ fm, where $V(R_x) = (-0.76 \pm 0.10)$ MeV. Good fits to the data have been obtained only with potentials which pass through this range of $V(R_x)$ values with relatively steep slopes, corresponding to $0.25 \text{ fm} \lesssim a_R \lesssim 0.50$ fm.

In addition to requiring significantly smaller values of a_R than are needed at the higher energies, the optical model analysis at 56 MeV also yields anomalously small values for the imaginary well diffuseness a_I (see Table IV). The variation in a_I suggests a strong energy dependence of the surface absorption strength. This is confirmed in Fig. 9, where the ratio W/V of imaginary to real depths evaluated at the s-wave barrier radius R_{B_0} is plotted for each of the potentials specified under procedure 1 in Table IV. The barrier radius is calculated for each potential from the condition

$$(dV_{\text{nucl}}/dr)_{r=R_{B_0}} = -(dV_{\text{Coul}}/dr)_{r=R_{B_0}} = Z_1 Z_2 e^2 / R_{B_0}^2 . \tag{13}$$

Although W/V at R_{B_0} is not tightly constrained by the analysis at any one energy, there is in Fig. 9 a clear energy dependence, consistent with that observed by Satchler[60] in his analysis of ^{16}O+Ni elastic scattering: W/V increases rapidly with energy at first and then appears to level off at the highest energies, presumably reflecting, at least in part, the behavior of the direct-reaction cross section. In light of this strong energy dependence at the low energies, it is not surprising that the energy-independent potentials obtained in procedure 2 provide a decidedly inferior fit to the 56-MeV data (see Fig. 4).

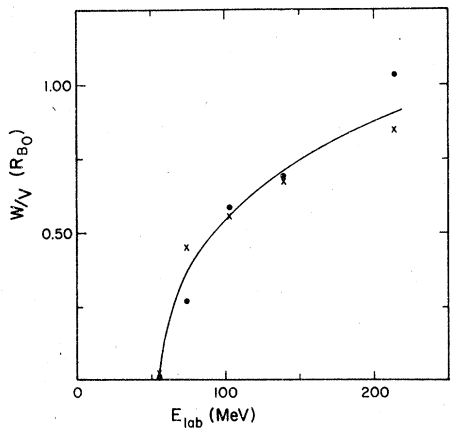

FIG. 9. Energy dependence of the ratio W/V of imaginary to real potential depths, evaluated at the $l = 0$ barrier position R_{B_0}, for the optical model potentials listed under procedure 1 in Table IV. The circles represent the potentials with $V_0 = 10$ MeV and the crosses those with $V_0 = 100$ MeV. The curve indicates a possible smooth energy dependence consistent with the plotted points within the expected uncertainty in the optical model determination of W/V.

All potentials which fit the elastic-scattering measurements at a given energy yield nearly the same values for the total reaction cross section and for the barrier penetration coefficients T_l as a function of l. In particular, the distinctly nonlinear dependence of σ_{reac} on $1/E_{\text{c.m.}}$ apparent over the broad energy range included in Fig. 5 is found using potentials obtained in any of the three search procedures described above. If σ_{reac} is interpreted in terms of a strong-absorption radius R_{SA}, via an expression similar to Eq. (5), then the observed nonlinearity reflects primarily a monotonic decrease in the value of R_{SA} with increasing energy. The sharp-cutoff approximation underlying an expression such as Eq. (5) is indeed found to reproduce the calculated values of σ_{reac} extremely well (at all energies except those barely exceeding the $l = 0$ potential barrier height) if the cutoff l value is identified as that ($l_{1/2}$) for which $T_l = 0.50$. [The values of $l_{1/2}$ and of $l_{1/4}$ from Eq. (2) are nearly identical in most cases.] R_{SA} then corresponds to the classical turning point for $l_{1/2}$, and is always somewhat larger than the radius at which the effective (nuclear + Coulomb + centrifugal) real potential (V_{eff}) for $l_{1/2}$ exhibits a barrier ($dV_{\text{eff}}/dr = 0$). The decrease in R_{SA} with increasing energy is not surprising since the radius of the potential barrier is known to decrease with increasing l.

Since R_{SA} is energy dependent, the "interaction barrier" parameters R_{INT}, V_{INT} which are often extracted from straight-line fits to low-energy σ_{reac} vs $1/E_{\text{c.m.}}$ data[11,33,64] bear no simple relation to the actual potential. This point is illustrated in Fig. 10, where it is shown that the point (R_{INT}, V_{INT}) determined by the conventional procedure from optical model reaction cross sections does not even come close to falling on the potential curve used to generate the fitted values of σ_{reac}.

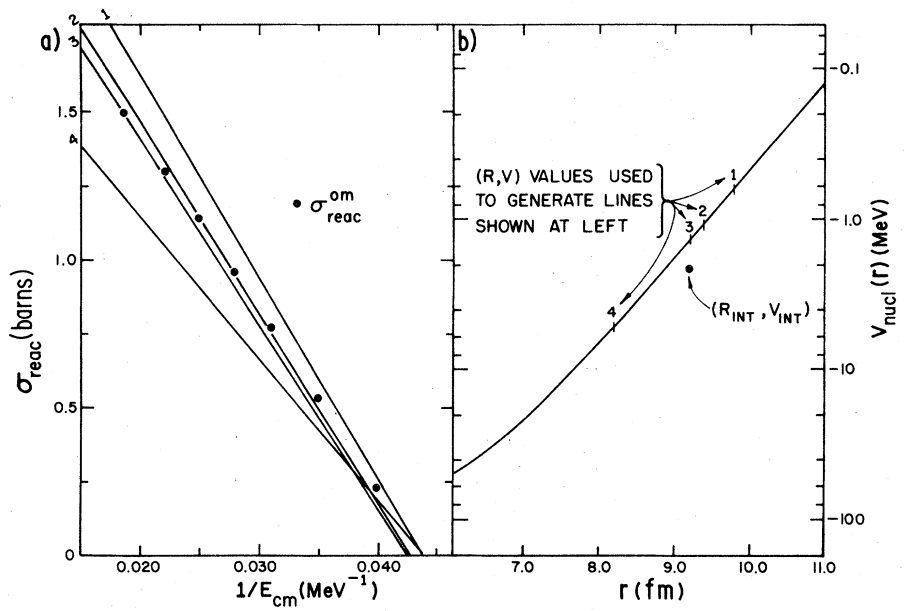

FIG. 10. Illustration of the error in "interaction barrier" parameters (R_{INT}, V_{INT}) extracted from straight-line fits to total reaction cross sections plotted vs $1/E_{c.m.}$. The σ_{reac} "data" in (a) were generated by optical model calculations using the energy-independent potential 2*b* of Table IV, whose real part is plotted in (b). The point (R_{INT}, V_{INT}) deduced from the best-fit straight line (not shown) to the data in (a) does not fall on the curve in (b). Conversely, various points on the potential curve in (b) define the unsatisfactory straight lines in (a).

The dependence of the barrier penetration coefficients T_l on l, as calculated for each energy with potential 2*a* (see Table IV), is shown in Fig. 11. In order to emphasize the increasing "diffuseness" of the T_l distributions with increasing energy, the curves at different energies have been shifted so that they all cross at $T_l = 0.75$ (i.e., when the elastic-scattering amplitude has magnitude $|\eta_l| = 0.50$). This value is chosen because it

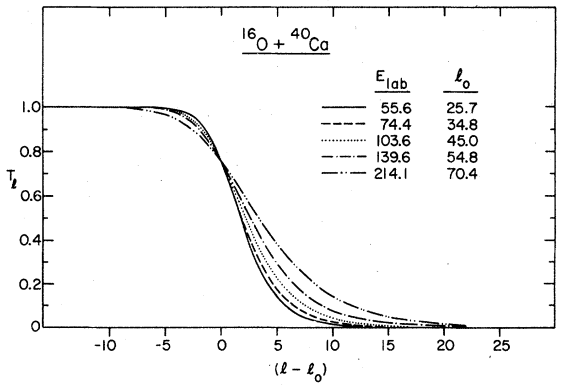

FIG. 11. Distributions of the barrier penetration coefficients T_l as a function of $(l - l_0)$ where $T_{l_0} = 0.75$, as determined from optical model calculations using potential 2*a* of Table IV. The value of l_0 at each energy is indicated in the figure.

corresponds closely at relatively low energies to the orbiting l value (l_{orb}),[57] for which the barrier height of the effective potential is just equal to $E_{c.m.}$. l space is then roughly divided into two regions,[57] corresponding on the one hand ($T_l > 0.75$) to classical "plunging" trajectories and more-or-less "violent" reactions, and on the other ($T_l < 0.75$) to "skimming" trajectories and peripheral reactions. We find that the diffuseness of the T_l distributions increases to just the extent necessary to maintain a constant value of the ratio $\sigma(T_l > 0.75)/\sigma_{reac} \simeq 0.87$, in contrast to the sharp decrease in $\sigma_{fus}/\sigma_{reac}$ evident for $E_{lab} \geq 75$ MeV in Fig. 5 and Table II. This observation suggests that the "missing" fusion strength at high energies is exhausted by other deep-penetration reactions, and is consistent with the critical-distance model. The T_l distributions thus do not explicitly reflect the dramatic change in the division of reaction strength which occurs over the energy range investigated.

E. Low-energy fusion cross sections and the nucleus-nucleus potential for $^{16}O + ^{40}Ca$

The energy dependence of fusion cross sections at energies significantly above the Coulomb barrier, but below the observed "bend" in σ_{fus} ($E_{c.m.}$), has often been treated[1-3,11,12,33,65] under assumptions analogous to those which lead to Eq. (5) for the high-energy fusion cross section. Thus, one as-

sumes a linear dependence on $1/E_{\text{c.m.}}$ with intercepts determined by R_{B_0}, V_{B_0}, the position and height of the $l=0$ potential barrier. However, for reasons analogous to those discussed above in the case of σ_{reac} data (see Fig. 10), the parameters extracted from such a straight-line fit to low-energy fusion measurements should *not* be interpreted as providing a *quantitative* description of the nucleus-nucleus potential. In the present section we investigate the possibility of extracting quantitative information concerning the potential from a more careful application of the basic premise that fusion arises from deeply penetrating trajectories. We are interested, in particular, in seeing whether one can construct a Woods-Saxon real potential capable of *simultaneously* fitting low-energy elastic-scattering and fusion data.

We begin by assuming that the product $T_l P_l$ of the barrier penetration and fusion probability coefficients has an l distribution similar to that for the T_l alone, but displaced toward lower l values. In particular, we assume that $T_l P_l$ reaches 0.50 for the orbiting partial wave l_{orb} (where T_l is usually $\simeq 0.75$), whereas $T_l = 0.50$ at $l_{1/2} > l_{\text{orb}}$. In other words, fusion exhausts half of the flux available in the partial wave which classically marks the dividing line between "skimming" and "plunging" trajectories.[57] The success of the sharp-cutoff approximation in reproducing optical model total reaction cross sections (see Sec. IV D) suggests that the analogous approximation should be valid for fusion cross sections at energies not too near the $l=0$ barrier:

$$\sigma_{\text{fus}} = \pi \lambda\!\!\!^{-2} l_{\text{orb}}(l_{\text{orb}}+1). \tag{14}$$

The energy dependence of the low-energy fusion cross section can now be calculated from Eq. (14) for any given nucleus-nucleus potential by determining the energy dependence of l_{orb} from the condition

$$E_{\text{c.m.}} = V_{\text{nucl}}(R_B) + \frac{Z_1 Z_2 e^2}{R_B} + \frac{l_{\text{orb}}(l_{\text{orb}}+1)\hbar^2}{2\mu R_B^{\,2}}, \tag{15}$$

where

$$(dV_{\text{nucl}}/dr)_{r=R_B} = \frac{Z_1 Z_2 e^2}{R_B^{\,2}} + \frac{l_{\text{orb}}(l_{\text{orb}}+1)\hbar^2}{\mu R_B^{\,3}} \tag{16}$$

and V_{nucl} represents the real nuclear potential. The use of the usual point-charge and point-mass expressions for the Coulomb and centrifugal potentials in Eqs. (15) and (16) is well justified in the surface region relevant to the present discussion. Equations (14)–(16) do not yield a strictly linear dependence of σ_{fus} on $1/E_{\text{c.m.}}$ since we have not introduced the usual additional assumption that the radius R_B of the potential barrier for l_{orb} remain constant at its $l=0$ value R_{B0}. In its explicit inclusion of the energy dependence of R_B, the approach outlined here is similar to that adopted by Bass.[15,30]

In applying Eqs. (14)–(16) we neglect the effect of any energy dissipation in the radial region *outside* the potential barrier ($r > R_B$). This assumption is generally made in analyses of low-energy fusion cross sections, but has recently been questioned by Birkelund and Huizenga.[65] The importance of surface friction must be related to the strength and average energy loss of direct reactions[39]; we expect that the neglect of friction at low energies for $^{16}\text{O}+^{40}\text{Ca}$ is justified because the measured total direct-reaction cross section at 56 MeV is relatively small and is dominated by transitions to low-lying states of the residual nuclei.[39] Furthermore, the effect on σ_{fus} of energy dissipation tends to be canceled at low energies by angular momentum dissipation.[19]

We now impose an additional constraint on the potentials used to calculate $\sigma_{\text{fus}}(E_{\text{c.m.}})$, namely, that they provide a good optical model fit to elastic-scattering data at energies within the low-energy fusion region. In thus introducing the assumption that a *single* potential should be able to account for both the elastic-scattering and the fusion measurements, we neglect not only the effects of friction on σ_{fus}, as discussed above, but also the effects of any explicit coupling of inelastic channels to the elastic scattering. It has recently been shown[66] that the backfeeding of specific transitions to the elastic channel is not necessarily simulated adequately by the absorptive term in a potential obtained from a conventional optical model analysis. It is hoped, however, that the alterations to the optical potential produced by such channel coupling are concentrated in the imaginary term,[66] with little effect on the real part, which is relevant for fitting $\sigma_{\text{fus}}(E)$. We also assume in our analysis that the real part of the potential is energy independent over the small range covered by the low-energy fusion data (40 MeV $\leq E_{\text{lab}} \leq$ 63 MeV). This is to be contrasted with the much broader assumptions concerning the energy or mass dependence of the potential which have been made in previous analyses aimed at extracting information on the nucleus-nucleus potential from elastic[32,67] or from fusion data[30,68] alone.

We find from our analysis that the calculated σ_{fus} $(E_{\text{c.m.}})$ is strongly correlated with the real well *diffuseness* of potentials which provide optimum fits to the 56-MeV elastic-scattering data. This correlation is demonstrated in Fig. 12(a), where we have plotted the mean percentage deviation (δ_{fus}) of the calculated from the measured low-energy fusion cross sections as a function of a_R for potentials within the two "families" discussed

previously in Sec. IV D (see Fig. 8). (We specify δ_{fus} rather than χ^2 for the fusion data, since χ^2 values are misleading when the experimental errors are predominantly systematic.) As the potential is varied, σ_{fus} $(E_{c.m.})$ calculated from Eqs. (14)–(16) tends to undergo overall upward or downward shifts, remaining in all cases essentially parallel to the curve representing potential $3a$ in Fig. 5. The calculated values of σ_{fus} exceed the measured values for *all* potentials obtained in the optical model analysis, with δ_{fus} falling below the mean fusion error bar (±5%) only for the largest values of a_R yielding acceptable elastic fits [see Fig. 12(a)].

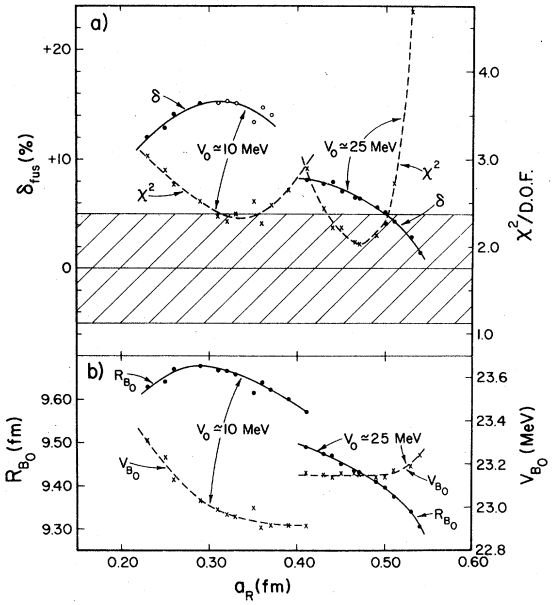

FIG. 12. (a) The variation with real well diffuseness a_R of the quality of fits provided to the 56-MeV elastic-scattering data and the low-energy fusion data for $^{16}O + ^{40}Ca$ by potentials belonging to two different families ($V_0 \simeq 10$ MeV and $V_0 \simeq 25$ MeV). The quality of elastic fit is specified by the value of χ^2 per degree of freedom (crosses and right-hand scale) while the quality of fusion fit is given by the mean percentage deviation (δ_{fus} — circles and left-hand scale) of the calculated from the measured values of σ_{fus} for 40 MeV $\leq E_{lab} \leq$ 63 MeV. The crosshatched region represents the mean size (±5%) of the error bars on the σ_{fus} measurements. The open circles for δ_{fus} represent potentials which do not yield an orbiting condition (i.e., potential "pockets") for energies up to $E_{lab} = 63$ MeV; δ_{fus} has been obtained for these from comparison of calculated and measured σ_{fus} at $E_{lab} \leq 56$ MeV. The curves are intended only to guide the eye. (b) The variation of the $l = 0$ barrier radius (R_{B_0}) and height (V_{B_0}) with a_R for the above two potential families. The curves are again only to guide the eye. Note the strong correlation between R_{B_0} and δ_{fus} plotted in (a).

As is seen in Fig. 12(a), δ_{fus} varies smoothly with a_R within each potential family, but jumps discontinuously from one family to the other. This behavior is related to that of the crossover of the real potentials (Fig. 8): As long as the potentials pass through a common crossover point, variation of their slope (a_R) results in a smooth variation of the $l = 0$ barrier parameters R_{B_0}, V_{B_0} [see Fig. 12(b)] and hence of σ_{fus} $(E_{c.m.})$.

By far the best *simultaneous* fits we have managed to obtain to the low-energy fusion and 56-MeV elastic-scattering data are those for potentials with $a_R = 0.50 \pm 0.05$ fm, $R_{B_0} = 9.38 \pm 0.07$ fm, $V_{B_0} = 23.17 \pm 0.07$ MeV. The real well depth and radius parameters are not well constrained by this analysis, since potentials related to one another by the Igo ambiguity[59] yield nearly identical elastic-scattering *and* fusion predictions. The most successful potentials in the $V_0 \simeq 25$ MeV family have unnaturally small imaginary well diffuseness values, $a_I \lesssim 0.05$ fm. We have chosen instead as our optimum potential ($3a$ in Table IV) one obtained by fitting the elastic data with a_I held fixed at the slightly more reasonable value 0.115 fm and a_R held fixed at 0.50 fm. This potential yields the very good fusion fit ($\delta_{fus} = 4.2\%$) shown in Fig. 5 and an elastic fit comparable to that obtained with the other four-parameter searches (potentials $1a1$ and $1a2$ in Table IV), but not quite as good as the best fits indicated in Fig. 12(a).

The real part of potential $3a$ has been used without modification in the third optical model search procedure discussed in Sec. IV D. As is clear from the χ^2 values specified for potentials $3a$–$3e$ in Table IV, the quality of fit obtainable for the elastic-scattering data with this real well deteriorates significantly by the highest energies, where the individual-energy optical model analyses suggest the need for larger values of the real diffuseness. If one accepts the fusion analysis as a reasonable means for choosing among otherwise "equivalent" optical potentials at low energies, then this deterioration of the procedure-3 fits at higher energies might reflect an energy dependence of the real potential, or perhaps the inadequacy of a Woods-Saxon shape.

In the low-energy region, it is clear from the present analysis that various potentials based on liquid-drop model (LDM) concepts,[28-30] which have been favored in recent global fusion analyses,[19,30,68] are much too diffuse to reproduce both the elastic and the fusion measurements for $^{16}O + ^{40}Ca$. This point is illustrated in Fig. 13, where the real part of potential $3a$ is compared to several proposed potentials[27-30] for $^{16}O + ^{40}Ca$. The Wilczynski potential[29] derived from LDM boundary conditions

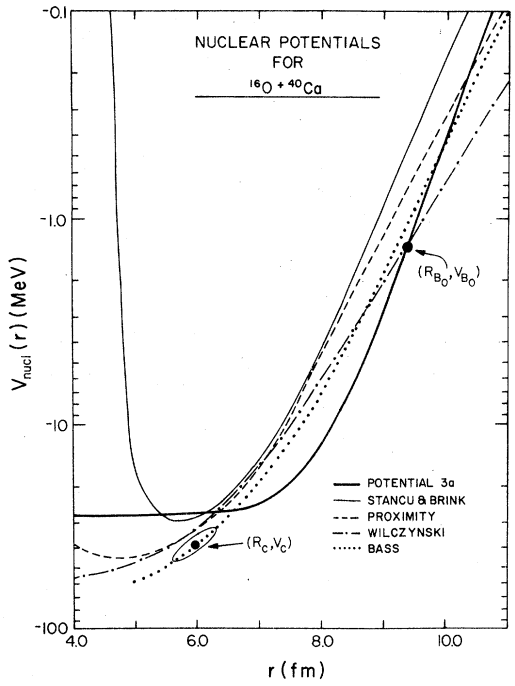

FIG. 13. Comparison of the optimum empirical real potential 3*a* with various proposed nucleus-nucleus potentials. Also indicated are the points (R_{B_0}, V_{B_0}) and (R_c, V_c^{nucl}) discussed in the text. The ellipse surrounding the latter point indicates the range of parameter values with which acceptable fits to the high-energy fusion data can be obtained in the critical-distance model.

has $a_R = 0.87$ fm. The proximity potential of Ref. 28 applied to $^{16}O + ^{40}Ca$ has an effective $a_R = 0.74$ fm, while the semiempirical Bass potential,[30] derived by fitting existing fusion data, has $a_R = 0.68$ fm. As indicated in Fig. 13, the Bass potential actually passes quite close to the points (R_{B_0}, V_{B_0}) and (R_c, V_c^{nucl}) (Ref. 69) which characterize our best fits to the low-energy and high-energy fusion data, respectively, and furthermore has $V(R_x = 9.7 \text{ fm})$ within the range appropriate to the 56-MeV best-fit optical potentials. Nonetheless, the Bass potential is much too diffuse to yield a good quantitative fit to the 56-MeV scattering data, and its incorrect slope in the surface region yields an $l = 0$ barrier at a radius 5% smaller than that for potential 3*a*, resulting in a significantly worse fit to the fusion data. The microscopic potential derived for $^{16}O + ^{40}Ca$ by Stancu and Brink[27] from a density-dependent effective nucleon-nucleon interaction has a more acceptable diffuseness, $a_R = 0.586$ fm, but much too small a value of $V(R_x)$, resulting in pathological elastic-scattering predictions. All of the above theoretical potentials conform rather well to a Woods-Saxon shape in the surface region, and it is thus unlikely that the discrepancies with the present results arise from our neglect of other shapes.

It is interesting that both the microscopic and macroscopic theoretical potentials considered in Fig. 13 are qualitatively consistent with (R_c, V_c^{nucl}), having depths between 29 and 38 MeV at the relevant radius. This observation provides some support for the essential validity of the critical-distance model of the limitation to high-energy fusion.

V. SUMMARY AND CONCLUSIONS

The striking qualitative behavior of the fusion excitation function observed for several lighter systems, with saturation setting in abruptly above a certain energy, has been shown to persist for $^{16}O + ^{40}Ca$. The present fusion data in this saturation region can be well reproduced in the simple critical-distance (R_c) model, using parameter values which are consistent with those obtained for other systems; the deduced potential depth (V_c^{nucl}) is consistent with a number of theoretical (both macroscopic and microscopic) nucleus-nucleus potentials. It seems necessary to expand the model, to allow comparison also with the energy systematics of *non*fusion reactions (probably requiring the inclusion of weak friction outside R_c), before a firmer conclusion on the validity of the critical-distance concept can be reached.

A number of other possible explanations for the saturation of σ_{fus} $(E_{\text{c.m.}})$ have been discussed and judged less satisfactory than the critical-distance model. For example, recently proposed mechanisms based on (a) a lower angular momentum cutoff[18,22,54] or (b) angular momentum dissipation and the disappearance of a potential "pocket"[19] appear to be seriously inconsistent with (a) the observed distribution of nonfusion reaction strength or (b) the observed extent of the fusion saturation energy region. In addition, the observed limitation on the high-energy fusion cross section for $^{16}O + ^{40}Ca$ is much more stringent than that which would be imposed by the yrast line predicted for the compound nucleus (^{56}Ni) in the rotating-liquid-drop model (RLDM).

The measured cross section for evaporation residues at $E_{\text{lab}} = 214$ MeV significantly exceeds the expectation based on the vanishing of the RLDM high-spin fission barrier. A perhaps related observation is that the extent of the laboratory angular distribution for fusion residues at 214 MeV suggests the onset of substantial pre-equilibrium emission of energetic α particles (or larger clusters) accompanying the formation of a long-lived composite system. Such pre-equilibrium emission is capable of removing sizable quantities of angular momentum, and thus might occur *instead* of fission. On the other hand, the present data do

not rule out the alternative possibility that such clusters are ejected from the regions of high density and temperature formed preferentially in collisions of *low* impact parameter.

While the high-energy fusion data may provide at best qualitative information on the depth of the nucleus-nucleus potential at small distances via the critical-distance model in its present simple form, we have reported the possibility that low-energy fusion measurements in combination with elastic-scattering data allow significant quantitative constraints to be placed on the potential in the surface region. Under the assumption that a single potential should be able to account for both sets of data, we have obtained good simultaneous fits to the 56-MeV elastic-scattering and low-energy fusion measurements with a Woods-Saxon real nuclear potential only when the diffuseness and barrier parameters are constrained to the ranges $a_R = 0.50 \pm 0.05$ fm, $R_{B_0} = 9.38 \pm 0.07$ fm, and $V_{B_0} = 23.17 \pm 0.07$ MeV. In fitting the fusion data it is *not* sufficient to use the usual straight-line approximation to the low-energy dependence of σ_{fus} on $1/E_{\text{c.m.}}$: The angular momentum (and hence energy) dependence of the potential barrier position must be taken into account explicitly.

The optimum value determined for the real well diffuseness in this simultaneous analysis of fusion and elastic scattering is considerably smaller than the values characteristic of various, currently favored, nucleus-nucleus potentials based on liquid-drop model (LDM) concepts.[28-30] This suggests either that very different effective real potentials are needed to account for elastic scattering and for fusion or that the LDM potentials are inapplicable at low energies.[70] The phenomenological real potential preferred at low energies does not provide good fits to the elastic-scattering measurements at the highest energies studied, where significantly larger real diffuseness values seem to be required. There also appears to be a significant energy dependence in the ratio of absorptive to real strengths in the surface region required for fitting the elastic-scattering data.

The present results suggest a number of related avenues for further investigation. Some of the following experiments are already in progress:

(1) Measurements of the fusion cross sections, along with transfer-reaction systematics, for $^{16}O + ^{40}Ca$ or similar systems, should be extended to still higher energies. Such data would reveal whether there is in fact a high-energy turnover in σ_{fus} $(E_{\text{c.m.}})$ corresponding to a fixed critical angular momentum J_{cr}, and if there is, how the experimental value of J_{cr} compares with the RLDM prediction. It is also of interest to see, with increasing energy, if pre-equilibrium emission grows in importance, further blurring the distinction between fusion and transfer products, and if transfer-reaction strength becomes more concentrated at *completely* damped energies.

(2) Fusion cross section data at high energies for alternative entrance channels to the compound nucleus ^{56}Ni (e.g., $^{32}S + ^{24}Mg$) should test the viability of all models in which the limitation on σ_{fus} is imposed by the structure of the compound nucleus.

(3) Angular correlations at high bombarding energy between light particles and "evaporation" residues should provide useful information on the mechanism of what we call "fusion." In particular, one would like to know whether the energetic clusters apparently emitted during "fusion" of $^{16}O + ^{40}Ca$ arise from low- or high-spin composite systems.

(4) Measurements of high-energy fusion cross sections for systems near in mass to $^{16}O + ^{40}Ca$, but which differ significantly in microscopic structure (e.g., $^{16}O + ^{44}Ca$, $^{18}O + ^{40,44}Ca$), will test for the presence of shell effects similar to those observed in lighter systems.[5,31]

(5) The simultaneous analysis of low-energy elastic-scattering and fusion data for other systems by the method outlined here (see also Ref. 34) will establish systematics on the extracted real well diffuseness values and should aid in evaluating the validity of the assumptions underlying this analysis.

The results of the present experiment, in conjunction with some or all of the above measurements, should place significant constraints on theoretical models for both the nucleus-nucleus potential and the mechanism responsible for the saturation of the fusion cross section and the onset of damped direct reactions in collisions of light- or medium-weight nuclei.

ACKNOWLEDGMENTS

We gratefully acknowledge the help of Dr. D. L. Hendrie in modifying the data acquisition program used for the Berkeley measurements. C. Ellsworth and G. E. Thomas devoted considerable effort to preparing the thin self-supporting calcium foils used in the experiment. This work was supported in part by the U. S. Energy Research and Development Administration and in part by the National Science Foundation.

*Present address: Physik-Department, Technische Universität München, Germany.
†Present address: Instituto de Fisica, U.N.A.M., Mexico.
‡Present address: Department of Physics, Indiana University, Bloomington, Indiana 47405.

[1]M. Lefort, Rep. Prog. Phys. 39, 129 (1976), and references therein.
[2]M. Lefort, J. Phys. A: Math. Nucl. Gen. 7, 107 (1974), and references therein.
[3]D. Glas and U. Mosel, Phys. Rev. C 10, 2620 (1974); Nucl. Phys. A237, 429 (1975).
[4]J. B. Natowitz, E. T. Chulick, and M. N. Namboodiri, Phys. Rev. C 6, 2133 (1972).
[5]P Sperr, S. Vigdor, Y. Eisen, W. Henning, D. G. Kovar, T. R. Ophel, and B. Zeidman, Phys. Rev. Lett. 36, 405 (1976); P. Sperr, T. H. Braid, Y. Eisen, D. G. Kovar, F. W. Prosser, Jr., J. P. Schiffer, S. L. Tabor, and S. Vigdor, *ibid.* 37, 321 (1976).
[6]M. N. Namboodiri, E. T. Chulick, and J. B. Natowitz, Nucl. Phys. A263, 491 (1976).
[7]R. G. Stokstad, J. Gomez del Campo, J. A. Biggerstaff, A. H. Snell, and P. H. Stelson, Phys. Rev. Lett. 36, 1529 (1976).
[8]J. B. Natowitz, in Proceedings of the Topical Conference on Heavy-Ion Collisions, Fall Creek Falls State Park, Tennessee, 1977 (ORNL Report CONF-770602, 1977), p. 115, and references therein.
[9]T. M. Cormier, A. J. Lazzarini, M. A. Neuhausen, A. Sperduto, K. Van Bibber, F. Videbaek, G. Young, E. B. Blum, L. Herried, and W. Thomas, Phys. Rev. C 13, 682 (1976); T. M. Cormier, in Proceedings of the Symposium on Macroscopic Features of Heavy-Ion Collisions, Argonne National Laboratory Report ANL/PHY-76-2, 1976 (unpublished), Vol. I, p. 153.
[10]K. L. Wolf and C. T. Roche, in Proceedings of the Symposium on Macroscopic Features of Heavy-Ion Collisions, Argonne National Laboratory Report ANL/PHY-76-2, 1976 (unpublished), Vol. I, p. 295.
[11]W. U. Schröder and J. R. Huizenga, Ann. Rev. Nucl. Sci. 27, 465 (1977), and references therein.
[12]J. Galin, D. Guerreau, M. Lefort, and X. Tarrago, Phys. Rev. C 9, 1018 (1974).
[13]D. Glas and U. Mosel, Phys. Lett. 49B, 301 (1974).
[14]D. Glas and U. Mosel, Nucl. Phys. A264, 268 (1976).
[15]R. Bass, Nucl. Phys. A231, 45 (1974).
[16]J. P. Bondorf, M. I. Sobel, and D. Sperber, Phys. Rep. 15, 83 (1974).
[17]D. H. E. Gross, H. Kalinowski, and J. N. De, *Lecture Notes in Physics, Classical and Quantum Mechanical Aspects of Heavy Ion Collisions*, edited by H. L. Harney, P. Braun-Munzinger, and C. K. Gelbke (Springer, Berlin, 1975), Vol. 33, p. 194.
[18]K. Siwek-Wilczynska and J. Wilczynski, Nucl. Phys. A264, 115 (1976).
[19]J. R. Birkelund, J. R. Huizenga, J. N. De, and D. Sperber, Phys. Rev. Lett. 40, 1123 (1978).
[20]M. Blann and F. Plasil, Phys. Rev. Lett. 29, 303 (1972); F. Plasil and M. Blann, Phys. Rev. C 11, 508 (1975).
[21]S. Cohen, F. Plasil, and W. J. Swiatecki, Ann. Phys. 82, 557 (1974).
[22]R. Y. Cusson, R. K. Smith, and J. A. Maruhn, Phys. Rev. Lett. 36, 1166 (1976); R. Y. Cusson, in Proceedings of the Topical Conference on Heavy-Ion Collisions, Fall Creek Falls State Park, Tennessee, 1977 (ORNL Report No. CONF-770602, 1977), p. 99.
[23]J. W. Negele, in Proceedings of the Topical Conference on Heavy-Ion Collisions, Fall Creek Falls State Park, Tennessee, 1977 (ONRL Report No. CONF-770602, 1977), p. 73.
[24]A. M. Zebelman and J. M. Miller, Phys. Rev. Lett. 30, 27 (1973).
[25]M. Lefort, Y. Le Beyec, and J. Péter, Riv. Nuovo Cimento 4, 79 (1974).
[26]A preliminary report of high-energy fusion measurements for $^{32}S+^{24}Mg$ has been given by D. G. Kovar, P. D. Bond, C. Flaum, M. J. LeVine, and C. E. Thorn, Bull. Am. Phys. Soc. 22, 66 (1977). Lower-energy measurements for this system were reported previously by H. H. Gutbrod *et al.*, Ref. 33.
[27]F. Stancu and D. M. Brink, Nucl. Phys. A270, 236 (1976).
[28]J. Blocki, J. Randrup, W. J. Swiatecki, and C. F. Tsang, Ann. Phys. (N.Y.) 105, 427 (1977).
[29]J. Wilczynski and K. Siwek-Wilczynska, Phys. Lett 55B, 270 (1975).
[30]R. Bass, Phys. Rev. Lett. 39, 265 (1977).
[31]R. G. Stokstad, in Proceedings of the Topical Conference on Heavy-Ion Collisions, Fall Creek Falls State Park, Tennessee, 1977 (ORNL Report No. CONF-770602, 1977), p. 22.
[32]It has been shown that there are no pronounced resonances in the fusion excitation function for $^{16}O+^{40}Ca$, in contrast to lighter systems of "α-particle nuclei," $^{16}O+^{12}C$, $^{12}C+^{12}C$, $^{16}O+^{16}O$, see D. F. Geesaman *et al.*, Phys. Rev. C 18, 284 (1978).
[33]H. H. Gutbrod, W. G. Winn, and M. Blann, Nucl. Phys. A213, 267 (1973); W. Scobel, H. H. Gutbrod, M. Blann, and A. Mignerey, Phys. Rev. C 14, 1808 (1976).
[34]L. C. Vaz, J. M. Alexander, and E. H. Auerbach, Phys. Rev. C 18, 820 (1978).
[35]Evidence for the observation of energetic α particles in coincidence with deeply inelastic products, possibly with preferential emission from the neck region of the composite system (at 90° to its major axis), has been reviewed recently in Ref. 31. See also J. M. Miller, G. L. Catchen, D. Logan, M. Rajagopalan, J. M. Alexander, M. Kaplan, and M. S. Zisman, Phys. Rev. Lett. 40, 100 (1978), and H. Ho *et al.*, Z. Phys. A283, 235 (1977).
[36]V. E. Viola, Jr., Nucl. Data 1, 391 (1966).
[37]B. Zeidman, W. Henning, and D. G. Kovar, Nucl. Instrum. Methods 118, 361 (1974).
[38]D. G. Kovar, Y. Eisen, W. Henning, T. R. Ophel, B. Zeidman, J. R. Erskine, H. T. Fortune, P. Sperr, and S. E. Vigdor, Phys. Rev. C 17, 83 (1978).
[39]S. E. Vigdor, in Proceedings of the Symposium on Macroscopic Features of Heavy-Ion Collisions, Argonne National Laboratory Report ANL/PHY-76-2, 1976 (unpublished), Vol. I, p. 95.
[40]D. G. Kovar, K. Daneshvar, P. Sperr, and S. E. Vigdor, Bull. Am. Phys. Soc. 22, 564 (1977), and to be published.
[41]J. S. Blair, Phys. Rev. 95, 1218 (1954).
[42]U. Mosel, T. D. Thomas, and P. Riesenfeldt, Phys. Lett. 33B, 565 (1970).

[43]C. W. Jager, H. deVries, and C. deVries, At. Data Nucl. Data Tables 14, 479 (1974).
[44]K. Neergard, V. V. Pashkevich, and S. Frauendorf, Nucl. Phys. A262, 61 (1976).
[45]G. E. Andersson, S. E. Larsson, G. Leander, P. Möller, S. G. Nilsson, I. Ragnarsson, S. Aberg, R. Bengtsson, J. Dudek, B. Nerlo-Pomorska, K. Pomorski, and Z. Szymanski, Nucl. Phys. A268, 205 (1976).
[46]F. Plasil, in *Proceedings of the International Conference on Reactions between Complex Nuclei, Nashville, Tennessee*, 1974, edited by R. L. Robinson, F. K. McGowan, J. B. Ball, and J. H. Hamilton (North-Holland, Amsterdam, 1974), Vol. 2, p. 107.
[47]J. R. Huizenga, Nukleonika 20, 291 (1975).
[48]R. G. Stokstad, R. A. Dayras, J. Gomez del Campo, P. H. Stelson, C. Olmer, and M. S. Zisman, Phys. Lett. 70B, 289 (1977).
[49]K. A. Geoffroy and J. B. Natowitz, Phys. Rev. Lett. 37, 1198 (1976).
[50]J. O. Newton, I. Y. Lee, R. S. Simon, M. M. Aleonard, Y. El Masri, F. S. Stephens, and R. M. Diamond, Phys. Rev. Lett. 38, 810 (1977).
[51]Calculations based upon a smooth transition in the P_2 are carried out by E. Seglie and D. Sperber [Phys. Rev. C 12, 1236 (1975)], but with the transition governed by the degree of overlap of the colliding nuclei at the distance of closest approach rather than by angular momentum dissipation.
[52]C. F. Tsang, Phys. Scr. 10A, 90 (1974).
[53]D. Horn and A. J. Ferguson, Phys. Rev. Lett. 41, 1529 (1978).
[54]R. A. Broglia, C. H. Dasso, G. Pollarolo, and A. Winther, Phys. Rev. Lett. 40, 707 (1978).
[55]A. J. Sierk and J. R. Nix, in Proceedings of the Symposium on Macroscopic Features of Heavy-Ion Collisions, Argonne National Laboratory Report ANL/PHY-76-2, 1976 (unpublished), Vol. I, p. 407.
[56]D. H. Gloeckner, N. H. MacFarlane, and S. C. Pieper, Argonne National Laboratory Report No. ANL-76-11, 1976 (unpublished).
[57]N. K. Glendenning, Rev. Mod. Phys. 47, 659 (1975).
[58]G. R. Satchler, in *Proceedings of the International Conference on Reactions between Complex Nuclei, Nashville, Tennessee*, 1974 edited by R. L. Robinson, F. K. McGowan, J. B. Ball, and J. H. Hamilton (North-Holland, Amsterdam, 1974), Vol. 2, p. 171.
[59]G. J. Igo, Phys. Rev. Lett. 1, 72 (1958).
[60]G. R. Satchler, Phys. Lett. 58B, 408 (1975).
[61]P. R. Christensen and A. Winther, Phys. Lett. 65B, 19 (1976).
[62]J. B. Ball, C. B. Fulmer, E. E. Gross, M. L. Halbert, D. C. Hensley, C. A. Ludemann, M. J. Saltmarsh, and G. R. Satchler, Nucl. Phys. A252, 208 (1975); W. Henning, Y. Eisen, J. R. Erskine, D. G. Kovar, and B. Zeidman, Phys. Rev. C 15, 292 (1977).
[63]F. Videbaek, R. B. Goldstein, L. Grodzins, S. G. Steadman, T. A. Belote, and J. D. Garrett, Phys. Rev. C 15, 954 (1977).
[64]L. C. Vaz and J. M. Alexander, Phys. Rev. C 10, 464 (1974).
[65]J. R. Birkelund and J. R. Huizenga, Phys. Rev. C 17, 126 (1978).
[66]K. E. Rehm, W. Henning, J. R. Erskine, and D. G. Kovar, Phys. Rev. Lett. 40, 1479 (1978).
[67]J. G. Cramer, R. M. DeVries, D. A. Goldberg, M. S. Zisman, and C. F. Maguire, Phys. Rev. C 14, 2158 (1976).
[68]K. Siwek-Wilczynska and J. Wilczynski, Phys. Lett. 74B, 313 (1978).
[69]We have used the prescription of Ref. 29 for the Coulomb potential between two overlapping nuclear charge distributions in extracting a value for the *nuclear* potential at the critical radius. A very similar result is obtained using instead the usual optical model prescription for the Coulomb potential.
[70]It is of course conceivable that we have extracted an anomalous value for the optimum real well diffuseness because of some anomaly in the interaction mechanism at 56 MeV, but there is little evidence to support this scenario. In particular, the small deviation of σ_{fus} at 56 MeV from the smooth trend established by the data at neighboring energies (see Fig. 5) is more likely a reflection of the measurement errors than of an anomaly in the mechanism, since a comparable deviation is not observed in the $^{16}O+^{40}Ca$ fusion excitation function reported in Ref. 32.